

# Quasinormal modes and excitation factors of Kerr black holes

Rico K. L. Lo,<sup>1,\*</sup> Leart Sabani,<sup>1,†</sup> and Vitor Cardoso<sup>1,2</sup>

<sup>1</sup>*Center of Gravity, Niels Bohr Institute, Blegdamsvej 17, 2100 Copenhagen, Denmark*

<sup>2</sup>*CENTRA, Departamento de Física, Instituto Superior Técnico – IST,*

*Universidade de Lisboa – UL, Avenida Rovisco Pais 1, 1049-001 Lisboa, Portugal*

(Dated: April 2, 2025)

Theoretical understanding of the characteristic oscillations of a perturbed black hole, also referred to as quasinormal modes (QNMs), is crucial to interpreting the late stage of binary black hole mergers that we now routinely observe in gravitational wave detectors. In this work, we introduce a new approach, based on the generalized Sasaki-Nakamura formalism, to compute the QNM spectra and their excitation factors (QNEFs), for scalar, electromagnetic and gravitational perturbations. Using this approach, QNM wavefunctions remain finite at the horizon and spatial infinity. Our results in general agree with previous calculations that were performed using different methods, though we further clarify that QNEFs and their scaling with the mass of the black hole depend on the spin-weight of the perturbation. We show that avoided crossing is *not* a general phenomenon: the real or the imaginary part of the eigenvalues can cross each other but not both simultaneously, and when crossing occurs in one part, repulsion follows in the another part. Eigenvalue repulsion, originating from branch point singularities, still plays an important role in the QNM spectra, despite the fact that the spectra depend only on the real-valued black hole angular momentum.

## I. INTRODUCTION

The geometry of an uncharged, rotating black hole (BH) in vacuum is described by the Kerr metric [1], and is characterized by its mass  $M$  and the angular momentum per unit mass  $a$  of the BH. When a BH is disturbed, it emits gravitational waves (GWs) during the relaxation process to a new equilibrium configuration. At late times the dynamics are well described by a linearization of Einstein equations. The characteristic frequencies of the corresponding problem are called the quasinormal modes (QNMs) of a BH; they are the characteristic oscillations excited whenever the BH interact with its exterior. For instance, the excited remnant formed after the merger of two BHs emits gravitational radiation composed primarily of QNMs to relax back to its stationary state. This was first detected by the Laser Interferometer Gravitational-Wave Observatory in 2015 [2]. With advancements in the sensitivity of these detectors, we might soon be able to perform BH spectroscopy [3, 4] measuring a number of distinct characteristic frequencies in the spectrum from GW data. The tantalizing prospect of actually doing BH spectroscopy, and the potential to uncover new physics, deserves a careful look at the problem, and indeed there is a vibrant activity in this topic [5, 6].

### A. Primer on black hole perturbation theory

Due to the lack of spherical symmetry of Kerr BHs, one would have speculated that the partial differential equations governing the linear perturbation of a field would

not be separable, i.e., the equation would be in general a partial differential equation of some variables, say the Boyer-Lindquist  $(t, r, \theta, \phi)$  coordinates [7, 8]. However, by considering instead some projections of the field, separation of variables on the governing wave equation of those scalar quantities can, surprisingly, be achieved [9]. The scalar quantity  $\psi^{(s)}$  to use depends on the nature of the perturbed field, the bracketed superscript  $s$  denotes its spin weight of the field ( $s = 0, \pm 1, \pm 2$  for scalar fields, electromagnetic fields and gravitational fields, respectively). If we further assume a harmonic time dependence  $\sim e^{-i\omega t}$  (where  $\omega$  for now is just a variable), then a wavefunction  $\psi^{(s)}$  can be written schematically as

$$\psi^{(s)}(t, r, \theta, \phi) = \sum_{\omega} \sum_{\ell m} {}_s R_{\ell m \omega}(r) {}_s S_{\ell m \omega}(\theta, \phi) e^{-i\omega t}, \quad (1)$$

where the indices  $\ell, m$  label angular wavefunctions  ${}_s S_{\ell m \omega}(\theta, \phi)$  and  ${}_s R_{\ell m \omega}(r)$  denotes a (time-independent) radial wavefunction. Focusing on the radial sector, the ordinary differential equation (ODE) that a radial wavefunction satisfies can be written as

$$\mathcal{L} [{}_s R_{\ell m \omega}] = \mathcal{S}, \quad (2)$$

where  $\mathcal{L}$  is a second-order linear differential operator representing the radial Teukolsky equation [9] and  $\mathcal{S}$  denotes the source term driving the perturbations. A number of techniques to solve the above equation have been developed over the years. One of those techniques is the Sasaki-Nakamura (SN) formalism [10–12], where Eq.(2) is transformed into a new ODE that is more suitable for direct numerical integrations. If  ${}_s X_{\ell m \omega}$  denotes a solution to this new ODE and  ${}_s \Lambda$  denotes an operator that transforms a radial Teukolsky solution  $R$  to the corresponding  $X$  solution (suppressing the  $s\ell m \omega$  subscripts whenever possible therein), then Eq. (2) can be recast simply as

$$\mathcal{L} [{}_s \Lambda^{-1} [{}_s X_{\ell m \omega}]] = \mathcal{S}, \quad (3)$$

\* kalok.lo@nbi.ku.dk

† leart.sabani@nbi.ku.dk

where  ${}_s\Lambda^{-1}$  denotes the inverse operator of  ${}_s\Lambda$  [12, 13].

To solve for generic cases where  $\mathcal{S} \neq 0$ , one can deploy the Green's function method [14]. Suppose  $u$  represents either  ${}_sR_{\ell m \omega}$  or  ${}_sX_{\ell m \omega}$  and  $u_{\text{in}, \text{out}}^\infty$ ,  $u_{\text{in}, \text{out}}^{\text{H}}$  denote solutions that solve Eq. (2) or Eq. (3) with  $\mathcal{S} = 0$  and satisfy the purely-in/outgoing boundary condition at spatial infinity and at the horizon, respectively. Furthermore, we construct two linearly independent solutions  $u_{\text{in}}$  and  $u_{\text{up}}$  from these solutions as

$$u_{\text{in}} = \begin{cases} u_{\text{in}}^{\text{H}} & \text{as } r_* \rightarrow -\infty \\ B^{\text{inc}} u_{\text{in}}^\infty + B^{\text{ref}} u_{\text{out}}^\infty & \text{as } r_* \rightarrow +\infty \end{cases}, \quad (4)$$

where the notation of  $A_{\text{in}} \equiv B^{\text{inc}}$  and  $A_{\text{out}} \equiv B^{\text{ref}}$  is also being used in literature on QNMs<sup>1</sup>, and

$$u_{\text{up}} = \begin{cases} C^{\text{ref}} u_{\text{in}}^{\text{H}} + C^{\text{inc}} u_{\text{out}}^{\text{H}} & \text{as } r_* \rightarrow -\infty \\ u_{\text{out}}^\infty & \text{as } r_* \rightarrow +\infty \end{cases}. \quad (5)$$

Here  $r_*$  is the tortoise coordinate related to the Boyer-Lindquist  $r$ -coordinate by

$$r_*(r) = r + \frac{2Mr_+}{r_+ - r_-} \ln \left( \frac{r - r_+}{2M} \right) - \frac{2Mr_-}{r_+ - r_-} \ln \left( \frac{r - r_-}{2M} \right), \quad (6)$$

where  $r_\pm = M \pm \sqrt{M^2 - a^2}$  is the outer and the inner horizon of the BH, respectively. More importantly, this coordinate transformation maps  $r = r_+$  into  $r_* \rightarrow -\infty$  while  $r \rightarrow \infty$  maps into  $r_* \rightarrow \infty$ .

More explicitly, the solution  ${}_sR_{\ell m \omega}$  of Eq. (2) with  $\mathcal{S} \neq 0$  on the right-hand side that satisfies the purely-ingoing boundary condition at the horizon and purely-outgoing boundary condition at spatial infinity can then be written, according to the theory of Green's functions [14], as

$${}_sR_{\ell m \omega}(r) = \frac{R_{\text{in}}(r)}{\mathcal{W}_R} \int_r^\infty dr' \frac{R_{\text{up}}(r') \mathcal{S}(r')}{\Delta^{-s}(r')} + \frac{R_{\text{up}}(r)}{\mathcal{W}_R} \int_{r_+}^r dr' \frac{R_{\text{in}}(r') \mathcal{S}(r')}{\Delta^{-s}(r')}, \quad (7)$$

where we have made the substitution of  $u \mapsto R$  and  $\Delta(r) \equiv r^2 - 2Mr + a^2$ . In the limit  $r \rightarrow \infty$  (appropriate for observers far away from the perturbed BH, e.g., us), using the expression of  $\mathcal{W}_R$  and  $R_{\text{up}}(r)$  in Ref. [12], we have

$$R(r \rightarrow \infty) = \left[ \frac{A_{\text{out}}^{\text{T}}}{2i\omega A_{\text{in}}^{\text{T}}} \int_{r_+}^\infty dr' \frac{R_{\text{in}}(r') \mathcal{S}(r')}{A_{\text{out}}^{\text{T}} \Delta^{-s}(r')} \right] r^{-(2s+1)} e^{i\omega r_*}, \quad (8)$$

where a superscript T is used to denote quantities related to Teukolsky solutions (similarly, we use a superscript SN

for quantities related to SN solutions). Notice that the term enclosed in the square bracket is independent of the field evaluation point  $r$ .

Putting Eq. (8) into Eq. (1) to get the full wavefunction  $\psi^{(s)}(t, r \rightarrow \infty, \theta, \phi)$  in the far field limit, we have

$$\psi^{(s)}(t, r \rightarrow \infty, \theta, \phi) = \sum_{\ell m} \int_{-\infty}^{+\infty} d\omega e^{i\omega r_* - i\omega t} {}_sS_{\ell m \omega}(\theta, \phi) \left[ \frac{A_{\text{out}}^{\text{T}}}{2i\omega A_{\text{in}}^{\text{T}}} \int_{r_+}^\infty dr' \frac{R_{\text{in}}(r') \mathcal{S}(r')}{A_{\text{out}}^{\text{T}} \Delta^{-s}(r')} \right] r^{-(2s+1)}. \quad (9)$$

In particular, we replace the schematic summation over  $\omega$  in Eq. (1) with the actual integral over  $\omega$ . Instead of evaluating the integral along the real line, one can evaluate an equivalent contour integral on the complex- $\omega$  plane [15].<sup>2</sup> Thanks to the residue theorem, part of the contour integral reduces to a much simpler discrete sum over the residues evaluated at the poles of the analytic integrand [17]. At some particular values of  $\omega$  referred to as QNM frequencies  $\omega_{\text{QNM}}$ ,  $A_{\text{in}}^{\text{T}} \equiv B_{\text{in}}^{\text{inc}}$  that appears in the denominator of the integrand vanishes (in fact, so as  $C_{\text{in}}^{\text{inc}}$ ). Mathematically, these are the poles of the Green's functions and will contribute to the sum. Physically, at those frequencies, the wavefunctions become purely ingoing at the horizon and outgoing at spatial infinity.

Let us write  $A_{\text{in}}(\omega)$  near those QNM frequencies as

$$A_{\text{in}}(\omega) = \underbrace{A_{\text{in}}(\omega_{\text{QNM}})}_{\neq 0} + \frac{0}{\frac{dA_{\text{in}}}{d\omega}} (\omega - \omega_{\text{QNM}}) + \dots, \quad (10)$$

we can then schematically write the sum over the QNM frequencies as

$$\psi^{(s)} \supset \sum_{\omega_n} 2\pi i \frac{A_{\text{out}}(\omega_n)}{2i\omega_n dA_{\text{in}}(\omega_n)/d\omega} E_n, \quad (11)$$

where  $n = 0, 1, \dots$  is the overtone number that labels the QNM frequencies by ascending  $|\text{Im } \omega_n|$  and  $E_n$  depends on the source term. For the particular  $s\ell m$  mode under consideration,  $\omega_0$  (or  $n = 0$ ) is referred to as the fundamental mode and  $\omega_{1,2,\dots}$  (or  $n = 1, 2, \dots$ ) are referred to as the overtones. Following the notations in Ref. [16], we define the part in Eq. (11) that is independent of the source term as the quasinormal excitation factor (QNEF)  $B_n$ , which is given by

$$B_n \equiv \frac{A_{\text{out}}}{2\omega} \left( \frac{dA_{\text{in}}}{d\omega} \right)^{-1} \Big|_{\omega=\omega_n}. \quad (12)$$

<sup>1</sup> We will use both notations interchangeably but never mix the two notations (so either  $A_{\text{in}, \text{out}}$  or  $B^{\text{inc}, \text{ref}}$  will appear together).

<sup>2</sup> Moreover, we choose a semi-circular contour going over the lower-half of the complex- $\omega$  plane with a branch cut starting at the origin along the negative imaginary axis. For an illustration, see Fig. 2 of Ref. [16].

Therefore, the accurate determination of the values of QNEFs is crucial in understanding QNM contents in the context of BH perturbation theory. There are already a large number of literature (e.g., Refs. [16–23]) on QNEFs of BHs in general relativity and some even beyond [24].

## B. This work

In this paper, we study QNM solutions of Kerr BHs and their QNEFs of perturbation fields with various spin weights ( $s = 0, \pm 1, \pm 2$ ) using the Generalized Sasaki-Nakamura (GSN) formalism [11, 12] that extends the original SN formalism to work for perturbations with any integer spin weight. Our work complements previous works mainly in two ways. First, we use the GSN formalism for numerical computations instead of the Mano-Suzuki-Takasugi (MST) method [20, 22] and a Heun-function-based method [21] that are deployed in some recent calculations of QNEFs in literature, allowing us to cross-check existing results. An underappreciated fact is that the QNEF defined in Eq. (12) under the Teukolsky formalism is actually *not* dimensionless, and the dimension depends on the spin weight  $s$ . Thus, care must be taken when using results computed with different conventions (e.g.,  $M = 1$  vs.  $M = 1/2$ ). Second, we compute both the  $+s$  and  $-s$  QNEFs explicitly for  $s = 0, 1, 2$  where they are in fact different even though they have identical QNM spectra, which is also underappreciated in literature.

This paper is structured as follows. In Sec. II, we develop the method to numerically solve the GSN equation for complex frequencies. Then in Sec. III, we specialize to QNMs, searching for the allowed complex frequencies and computing their corresponding QNEFs. We discuss our results in Sec. IV, and summarize our findings in Sec. V.

Throughout this paper, we use geometric units  $c = G = M = 1$ . As a result, the Teukolsky excitation factors reported here coincide with the dimensionless  $M^{-2s} B_n^{T,(s)}$ .

## II. GENERALIZED SASAKI-NAKAMURA FORMALISM WITH COMPLEX FREQUENCIES

Before we embark on the journey of computing QNM solutions using the GSN formalism, let us first review the essence of the procedure (we refer readers to Ref. [12] for a detailed account of the GSN formalism). We then describe how a standard trick in the theory of complex variables (i.e., deforming the integration contour) allows us to numerically solve the GSN equation with complex frequencies.

Instead of solving for the Teukolsky function, we solve

for the GSN function  $X(r_*)$ , which satisfies the ODE

$$\frac{d^2 X}{dr_*^2} - \mathcal{F} \frac{dX}{dr_*} - \mathcal{U} X = 0, \quad (13)$$

where the potentials  $\mathcal{F}$  and  $\mathcal{U}$  are functions of the BH parameters, the radial coordinate, the angular numbers characterizing the angular distribution of the field, and of the frequency  $\omega$ . The frequency  $\omega$  can be interpreted either physically as the wave frequency near spatial infinity or mathematically as the Fourier variable.

In particular, let us examine the asymptotic behaviors of GSN functions as  $r_* \in \mathbb{R} \rightarrow \pm\infty$ . They behave like

$$X \rightarrow \begin{cases} \exp(\pm i p r_*) & \text{as } r_* \rightarrow -\infty \\ \exp(\pm i \omega r_*) & \text{as } r_* \rightarrow +\infty \end{cases}, \quad (14)$$

where  $p \equiv \omega - ma/(2r_+)$  is the “effective wave frequency” at the BH horizon. If the imaginary part of  $\omega$  is negative, then  $X \sim e^{\pm |\text{Im } \omega| r_*} e^{\pm i(\text{Re } \omega) r_*}$  as  $r_* \rightarrow \infty$ . This means that the wave amplitude is either exponentially growing or exponentially decaying, depending on the wave propagation direction. The same phenomenon occurs when  $r_* \rightarrow -\infty$ , with  $X \sim e^{\pm |\text{Im } \omega| r_*} e^{\pm i[(\text{Re } \omega) - ma/(2r_+)] r_*}$ . This makes accurate numerical integration of the GSN equation and the determination of the asymptotic amplitudes particularly challenging, even though the formalism itself works just fine with a complex  $\omega$ .

In fact, this exponential growth or decay in the amplitude of the GSN function is simply a coordinate artifact. By analytic-continuing the GSN function  $X(r_*)$  from the real line to the entire complex- $r_*$  plane and integrating Eq. (13) along a deformed contour on the complex plane<sup>3</sup>, one can suppress this coordinate artifact and the GSN equation will still admit a plane-wave solution with unit amplitude when  $|r_*| \rightarrow \infty$ .<sup>4</sup>

### A. Analytic continuation of the Boyer-Lindquist- $r$ coordinate

Recall that the Boyer-Lindquist  $r$ -coordinate is related to the tortoise coordinate  $r_*$  introduced earlier in Eq. (6) (for real values of  $r$  and  $r_*$ ) by

$$\frac{dr}{dr_*} \equiv \frac{\Delta(r)}{r^2 + a^2}. \quad (15)$$

<sup>3</sup> In the context of BH perturbation theory, this has already been employed in, for example, Refs. [18, 25]. It has also been adopted to study scattering processes in non-Hermitian quantum mechanics, known as the complex scaling transformation [26, 27], that transforms resonances states into bound states.

<sup>4</sup> Another way to suppress this artifact is to use a set of horizon-penetrating hyperboloidally-compactified coordinates. See, for example, Ref. [28].

We shall use this relation and Eq. (6) to analytic-continue  $r(r_*)$  for complex values of  $r_*$ . Instead of using the real and the imaginary part of  $r_*$ , we parametrize  $r_*$  as

$$r_* = r_*^{\text{mp}} + \rho e^{i\beta}, \quad (16)$$

where  $r_*^{\text{mp}}$  is a real number and  $\rho \in (-\infty, +\infty)$ ,  $|\beta| < \pi/2$  are two real variables.

With this parametrization, we can use the notion of a differential in the usual sense, i.e., an infinitesimally small change of a variable. Along a path  $C_\rho$  with varying  $\rho$  but  $\beta$  unchanged (say,  $\beta = \beta_0$ ), we have

$$dr_* = e^{i\beta_0} d\rho. \quad (17)$$

Similarly, along a path  $C_\beta$  with varying  $\beta$  but  $\rho$  unchanged (say,  $\rho = \rho_0$ ), we have

$$dr_* = i\rho_0 e^{i\beta} d\beta. \quad (18)$$

For instance, the path  $C_\rho$  shown in Fig. 1 can be parametrized by  $r_*(\rho)$  with a fixed  $\beta$ , while the path  $C_\beta$  in the same figure can be parametrized by  $r_*(\beta)$  with a fixed  $\rho$ .

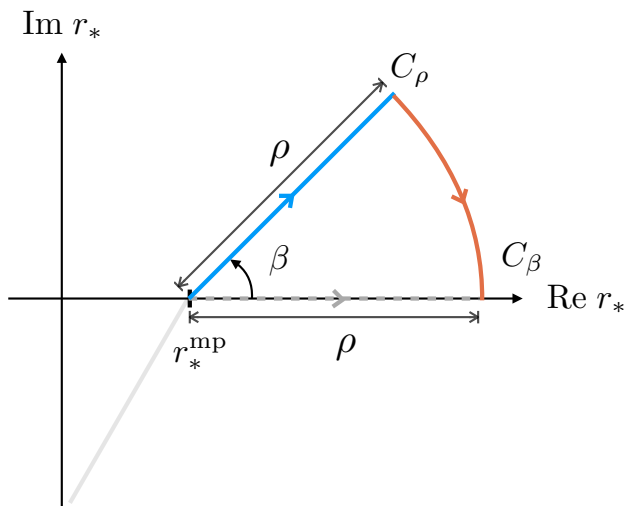


FIG. 1. Complex- $r_*$  plane parametrized by two real variables  $\rho$  and  $\beta$ .

We solve for  $r(\rho)$  by integrating the ODE obtained from substituting Eq. (17) into Eq. (15), which is

$$\frac{dr}{d\rho} = e^{i\beta_0} \frac{\Delta(r)}{r^2 + a^2}, \quad (19)$$

together with the initial condition that  $r = r(r_*^{\text{mp}} \in \mathbb{R})$  given by the inverse of Eq. (6)<sup>5</sup> when  $\rho = 0$  (hence the superscript mp, which stands for matching point). Figure 2 shows an example of  $r(\rho)$  (blue solid curve) with

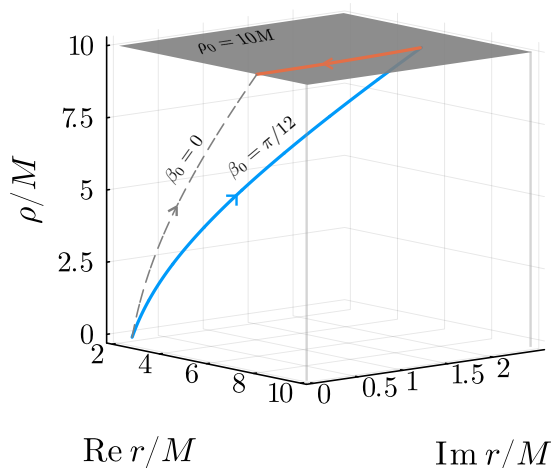


FIG. 2. An example of  $r(\rho)$  (blue solid curve) and  $r(\beta)$  (orange solid curve), respectively, with  $r_*^{\text{mp}} = 0$ ,  $a = 0$ . In particular we are showing  $r(\rho)$  with  $\beta_0 = \pi/12$  from the matching point  $\rho = 0$  up to  $\rho = 10$ . At  $\rho_0 = 10$ ,  $r(\beta)$  connects  $r(\rho = 10) \in \mathbb{C}$  with  $r(r_* = 10) \in \mathbb{R}$ , demonstrating the path independence of  $\int dr/dr_*$  as required by the analyticity of  $r(r_* \in \mathbb{C})$ .

$\beta_0 = \pi/12$ ,  $r_*^{\text{mp}} = 0$ ,  $a = 0$  and  $\rho \in [0, 10]$ . It diverges from  $r(r_* \in \mathbb{R})$  (grey dashed curve), i.e.,  $\beta_0 = 0$ , starting at the matching point ( $\rho = 0$ ). In the same figure, we also show  $r(\beta)$  (orange solid curve) with  $\rho_0 = 10$  and  $\beta \in [0, \pi/12]$ . We see that it connects  $r(r_* = 10e^{i\pi/12})$  to  $r(r_* = 10)$  as required by the analyticity of  $r(r_* \in \mathbb{C})$ .

## B. Analytic continuation of the generalized Sasaki-Nakamura functions

Equipped with the analytic-continued  $r(r_*)$ , we can analytic-continue also the GSN potentials  $\mathcal{F}(r_*)$  and  $\mathcal{U}(r_*)$  by evaluating these potentials at complex values of  $r = r(r_* \in \mathbb{C})$ .<sup>6</sup> Following that, we can analytic-continue GSN functions  $X(r_*)$  by integrating Eq. (13). Since numerically it is easier to integrate an ODE of a real variable instead of a complex one, we adopt the parametrization in Eq. (16) and vary  $\rho$  or  $\beta$  at a time.

### 1. Varying $\rho$

Along the  $C_\rho$  path,  $\rho$  is the variable with  $\beta = \beta_0$  held fixed. Substituting Eq. (17) into Eq. (13), we have

$$\frac{d^2 X}{d\rho^2} - e^{i\beta_0} \mathcal{F} \frac{dX}{d\rho} - e^{2i\beta_0} \mathcal{U} X = 0, \quad (20)$$

<sup>5</sup> Note that  $r(r_* \in \mathbb{R})$  is multivalued. Here we choose the branch that maps  $r_* \in (-\infty, +\infty) \mapsto r \in (r_+, \infty)$ .

<sup>6</sup> Note that these functions have poles located at  $r = \pm ia$ . Since these poles are not in the image of  $r(r_*)$ , those functions are still analytic in  $r_*$ .

which is different from the original GSN equation. However,  $X(\rho)$  is still a solution to the original GSN equation evaluated at  $X(r_* = r_*^{\text{mp}} + \rho e^{i\beta_0})$ .

Notice that Eq. (20) is almost identical to the original GSN equation in Eq. (13) by rescaling the potentials as

$$\tilde{\mathcal{F}}(\rho) \equiv e^{i\beta} \mathcal{F}(r(\rho)), \quad (21)$$

$$\tilde{\mathcal{U}}(\rho) \equiv e^{2i\beta} \mathcal{U}(r(\rho)). \quad (22)$$

Therefore, the transformed GSN equation can be written as

$$\frac{d^2 X}{d\rho^2} - \tilde{\mathcal{F}} \frac{dX}{d\rho} - \tilde{\mathcal{U}} X = 0. \quad (23)$$

We can also reuse *exactly* the ansatzes constructed for the original GSN equation in Ref. [12] to help solve this new equation. Note that we will need  $\{X, dX/d\rho\}$  instead of  $\{X, dX/dr_*\}$ , but the derivative  $dX/d\rho$  is related to  $dX/dr_*$  by

$$\begin{aligned} \left. \frac{dX}{d\rho} \right|_{\rho=\rho_0} &= \left. \frac{dr_*}{d\rho} \frac{dX}{dr_*} \right|_{r_*=r_*^{\text{mp}}+\rho_0 e^{i\beta}} \\ &= e^{i\beta} \left. \frac{dX}{dr_*} \right|_{r_*=r_*^{\text{mp}}+\rho_0 e^{i\beta}}, \end{aligned} \quad (24)$$

which is nothing but the chain rule written out explicitly.

Asymptotically as  $\rho \rightarrow \pm\infty$ , we see that the solutions  $\tilde{X}$  behave as

$$X(\rho) \rightarrow \begin{cases} \exp[\pm i(e^{i\beta} p)\rho] & \text{as } \rho \rightarrow -\infty \\ \exp[\pm i(e^{i\beta} \omega)\rho] & \text{as } \rho \rightarrow +\infty \end{cases}. \quad (25)$$

If we choose  $\beta$  carefully such that the combination  $e^{i\beta}\omega$  or  $e^{i\beta}p$  is a purely real number, then asymptotically  $X(\rho)$  will behave like a plane wave of constant amplitude even with a complex  $\omega$ .

Recall that we can express any complex number  $k$  as

$$k = |k|e^{i \arg k}. \quad (26)$$

Therefore, if we choose  $\beta = -\arg k$ , where  $k$  can be  $\omega$  or  $p$  as appropriate, then

$$e^{i\beta} k = e^{-i \arg k} k = (k^*/|k|)k = |k|^2/|k| = |k|, \quad (27)$$

where a superscripted asterisk denotes the complex conjugate, is indeed a purely real number.

Since  $p$  coincides with  $\omega$  only when  $m = 0$  or  $a = 0$ , we need to deform the integration contour into two broken line segments (i.e., with two different slopes, given precisely by  $\beta$ ) in the complex- $r_*$  plane in generic cases. The appropriate choices of  $\beta$  are as follows – when  $\rho < 0$

$$\beta = \begin{cases} -\arg p & \text{when } \text{Re } p > 0 \\ -\arg p + \pi & \text{when } \text{Re } p < 0 \end{cases}, \quad (28)$$

and when  $\rho > 0$ , we have

$$\beta = \begin{cases} -\arg \omega & \text{when } \text{Re } \omega > 0 \\ -\arg \omega + \pi & \text{when } \text{Re } \omega < 0 \end{cases}. \quad (29)$$

In particular,  $\beta$  is always within the allowed range  $(-\pi/2, \pi/2)$  with these choices.<sup>7</sup> Note that adding an extra  $\pi$  to  $\beta$  is identical to flipping  $\rho \mapsto -\rho$  as  $e^{i\pi} = -1$ .

## 2. Varying $\beta$

Along the  $C_\beta$  path,  $\beta$  is the variable with  $\rho = \rho_0$  held fixed instead. Substituting Eq. (18) into Eq. (13), the new ODE that needs to be solved reads

$$\frac{d^2 X}{d\beta^2} - i(1 + \rho_0 e^{i\beta} \mathcal{F}) \frac{dX}{d\beta} + (\rho_0 e^{i\beta})^2 \mathcal{U} X = 0. \quad (30)$$

The derivative  $dX/d\beta$  is *no longer* a simple constant rescaling of  $dX/dr_*$  compared to  $dX/d\rho$ . In particular, when  $|\rho_0| \rightarrow \infty$ , the ODE simplifies drastically as the potentials approach

$$\begin{aligned} \mathcal{F} &\rightarrow 0 & \text{as } \rho \rightarrow \pm\infty, \\ \mathcal{U} &\rightarrow \begin{cases} -p^2 & \text{as } \rho \rightarrow -\infty \\ -\omega^2 & \text{as } \rho \rightarrow +\infty \end{cases}. \end{aligned} \quad (31)$$

The ODE can be solved analytically in this limit as

$$X(\beta) = c_1 \exp(ik\rho_0 e^{i\beta}) + c_2 \exp(-ik\rho_0 e^{i\beta}), \quad (32)$$

where  $c_{1,2}$  are some constants to be determined by the initial conditions at  $\beta = \beta_0$  and that  $k = \omega$  when  $\rho_0 \rightarrow \infty$  and  $k = p$  when  $\rho_0 \rightarrow -\infty$ . For example, when  $\rho_0 \rightarrow \infty$  we have

$$X(\rho_0 \rightarrow \infty, \beta_0) = c_1 \exp(i\omega\rho_0 e^{i\beta_0}) + c_2 \exp(-i\omega\rho_0 e^{i\beta_0}). \quad (33)$$

When  $\beta = 0$ , i.e.,  $r_* = r_*^{\text{mp}} + \rho_0$  is purely real, the solution becomes

$$\begin{aligned} X(\rho \rightarrow \pm\infty, \beta = 0) &= c_1 \exp[ik(r_* - r_*^{\text{mp}})] \\ &\quad + c_2 \exp[-ik(r_* - r_*^{\text{mp}})] \\ &= \underbrace{c_1 e^{-ikr_*^{\text{mp}}}}_{A_{\text{out}}} e^{ikr_*} + \underbrace{c_2 e^{ikr_*^{\text{mp}}}}_{A_{\text{in}}} e^{-ikr_*}. \end{aligned} \quad (34)$$

This is a key result – it means that we can extract the asymptotic amplitudes  $A_{\text{in}}$  and  $A_{\text{out}}$  of  $X(r_*)$  directly from the asymptotic amplitudes  $c_1$  and  $c_2$  of  $X(\rho)$ , where  $X(\rho)$  can be solved accurately (see, for example, Ref. [12]) with an off-the-shelf numerical integrator.

We now have everything needed to compute  $A_{\text{in}}(\omega)$  and  $A_{\text{out}}(\omega)$  for a complex  $\omega$ , where a Kerr QNM is a solution to the GSN equation in Eq. (13) with a vanishing  $A_{\text{in}}$ .

<sup>7</sup> These choices, therefore, do not work for purely imaginary modes (e.g., see Ref. [29]) where the real part of  $\omega$  or  $p$  vanishes as  $\beta$  would be  $\pm\pi/2$ .

### III. RESULTS

We are now ready to compute QNM solutions of Kerr BHs using the GSN formalism we have just developed. In Sec. III A, we first solve  $X_{\text{in}}$  and  $X_{\text{up}}$  [cf. Eqs. (4) and (5)] for some complex frequencies. Then, in Sec. III B, we search for QNM frequencies  $\omega_{\text{QNM}}$  recovering previous results [5, 30–32], while extending most of them to higher BH rotation. Using these values of the QNM frequencies, in Sec. III C, we compute the QNEF for each of those modes as defined in Eq. (12).

Numerically, the radial Teukolsky and the GSN equations are solved with a `julia` [33] implementation of the GSN formalism in `GeneralizedSasakiNakamura.jl` [12].<sup>8</sup> In particular, they are solved with the `Vern9` algorithm [34] implemented in `DifferentialEquations.jl` [35] and double-precision floating-point numbers. As for the angular Teukolsky equation, we use a spectral decomposition method [32, 36] implemented in `SpinWeightedSpheroidalHarmonics.jl` [12],<sup>9</sup> which works with complex frequencies. In particular, we optimize  $r_*^{\text{mp}}$  [cf. Eq. (16)] for each mode such that the matching point is as close to the horizon as possible for a better computation efficiency (see Appendix A).

#### A. Solutions to the generalized Sasaki-Nakamura equation

To obtain  $X_{\text{in}}$ , for example, we integrate Eq. (20) from  $r_*^{\text{in}} = r_*^{\text{mp}} + \rho_{\text{in}} e^{i\beta(\rho_{\text{in}})}$ , where  $\rho_{\text{in}} < 0$  and  $\beta(\rho_{\text{in}})$  is determined by Eq. (28), to  $\rho = 0$  (which is at  $r_* = r_*^{\text{mp}}$ ) with  $\beta$  held fixed. We then continue the integration from  $\rho = 0$  to  $\rho = \rho_{\text{out}} > 0$  [correspondingly,  $r_* = r_*^{\text{mp}} + \rho_{\text{out}} e^{i\beta(\rho_{\text{out}})}$ ] along a *different* constant- $\beta$  direction where  $\beta = \beta(\rho_{\text{out}})$  is determined by Eq. (29). Similarly for  $X_{\text{up}}$ , we integrate Eq. (20) from  $\rho_{\text{out}} > 0$  to 0 with  $\beta = \beta(\rho_{\text{out}})$ , and then from 0 to  $\rho_{\text{in}} < 0$  with  $\beta = \beta(\rho_{\text{in}})$ .

An example of  $X_{\text{in}}$  with  $s = -2, \ell = m = 2, a = 0.68$  and  $\omega = 0.5239751 - 0.0815126i$  is shown in Fig. 3. As expected,  $X_{\text{in}}(\rho)$  in the upper panel behaves like a plane wave near the two boundaries, while  $X_{\text{in}}(r_*)$  in the lower panel exhibits an exponential blow up in the amplitude near  $r_* \rightarrow \infty$ , following the expected  $e^{|\text{Im}\omega|r_*}$  scaling (gray dashed line).

In theory, for each value of  $\rho = \rho_0$ , we integrate Eq. (30) from  $\beta = \beta(\rho_0)$  back to  $\beta = 0$  on the real axis. In practice, we are mostly interested in the asymptotic values when  $r_* \rightarrow \pm\infty$ . In this case, Eq. (32) gives the desired solution with two constants  $c_{1,2}$  determined by the asymptotic solutions  $X_{\text{in}}(\rho)$ . We follow the procedures given in Sec. III B of Ref. [12], i.e., matching the

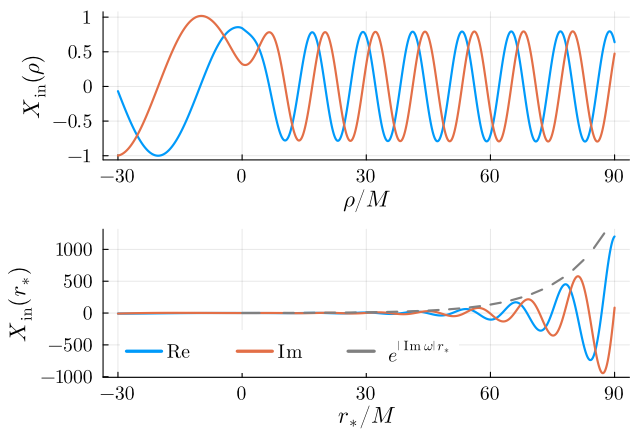


FIG. 3. GSN solution  $X_{\text{in}}$  with  $s = -2, \ell = m = 2, a/M = 0.68$  and  $M\omega = 0.5239751 - 0.0815126i$  along a deformed integration contour parametrized by  $\rho$  (upper panel) and along the real axis of  $r_*$  (lower panel), respectively.

numerical solution of  $X_{\text{in}}$  that was solved up to a numerical outer boundary at  $\rho = \rho_{\text{out}}$  with an analytical ansatz, to extract the values of  $c_{1,2}$  and then  $A_{\text{out}}$  and  $A_{\text{in}}$  using Eq. (34).

For instance, with the example shown in Fig. 3, the reflection amplitude  $A_{\text{out}}$  is about  $-0.801 + 0.0291i$ ,<sup>10</sup> while the incidence amplitude  $A_{\text{in}}$  is about  $-1.51 \times 10^{-7} - 7.98 \times 10^{-8}i$ . It is no coincidence that  $A_{\text{in}}$  here is tiny – this particular frequency was chosen to be very close to the fundamental mode for the  $|s| = \ell = m = 2$  QNM.

#### B. Quasinormal mode frequencies

To establish the QNM frequency spectrum for a perturbation field of spin weight  $s$  and angular mode labeled by  $(\ell, m)$ , we solve the nonlinear equation  $A_{\text{in}}(\omega_{\text{QNM}}) = 0$  for  $a/M \in [0, 1)$  using the Newton-Raphson method [37]. While verifying a QNM frequency can be done very quickly, the tabulation of those frequencies for different  $s\ell m$  modes, on the other hand, is a time-consuming task.

Fortunately, one can save computational time by exploiting symmetries and identities of homogeneous solutions to the Teukolsky equation. For instance, perturbations of spin weight  $s$  and  $-s$  share the same QNM frequency spectrum. This is because asymptotic amplitudes of a homogeneous solution with spin weight  $s$  are proportional to that of  $s \mapsto -s$  by the virtue of the Teukolsky-Starobinsky identities [38, 39]. Therefore, when tabulating QNM frequencies, one only needs to compute values either with  $s$  or  $-s$ .

Another useful relation is that

$$s u_{\ell, m, -\omega^*} = s u_{\ell, -m, \omega}^*, \quad (35)$$

<sup>8</sup> <https://github.com/ricokaloklo/GeneralizedSasakiNakamura.jl> from v0.6.0 onward.

<sup>9</sup> <https://github.com/ricokaloklo/SpinWeightedSpheroidalHarmonics.jl>.

<sup>10</sup> We are showing these numbers to 3 significant figures only for demonstration purposes.

where  $u$  can be either a homogeneous solution to the radial Teukolsky equation,  $R$ , or that to the GSN equation,  $X$ . This implies that for a given  $s\ell m$  mode, one only needs to compute QNM frequencies, for example, with a positive real part, and the rest of the spectrum can be “mirrored” (flipping only the sign of the real part) from the corresponding  $-m$  mode. More explicitly, if we denote those QNM frequencies with a positive real part as  $\{\omega_{s\ell mn}^+\}$ , which are sometimes referred to as “ordinary” modes, then there is also another set of QNM frequencies given by  $\{\omega_{s\ell mn}^- \equiv -\omega_{s\ell(-m)n}^+\}$ , which are also referred to as mirror modes in literature.

In this work, we tabulate QNM frequencies from the nonspinning limit with  $a = 0$  to the near-extremal limit with  $a = 1 - 10^{-4}$ , and  $|s| \leq \ell \leq 7$ ,  $-\ell \leq m \leq \ell$ ,  $n \leq 3$  for both scalar<sup>11</sup> and electromagnetic QNMs (i.e.,  $s = 0, \pm 1$ , respectively) and  $n \leq 7$  for gravitational QNMs (i.e.,  $s = \pm 2$ ). We only explicitly compute QNM frequencies where their real part are positive. These tables are available online – see [Data Availability](#).

It is important to note that most of the QNMs tabulated in this work have been previously computed and that our main goal here is to cross-check the frequency calculations. As an example, Fig. 4 shows the trajectory in the complex plane, parametrized by  $a$ , of the  $s = \ell = m = 0, n = 1$  QNM frequencies obtained in this work (blue), using the `qnm` package [40] (orange) and from Berti *et al.* [3, 5] (green), respectively. The three trajectories agree well for most values of  $a$ . Discrepancies only begin at near-extremal spins  $a \gtrsim 0.99$ , where our calculation suggests that the QNM frequency approaches steadily to  $\omega \approx 0.0625 - 0.3188i$  at  $a = 0.9999$ , which matches with the value presented in Table I of Ref. [41] for the extremal  $a = 1$  case (open circle in the inset of Fig. 4) when rounded to the same precision. On the other hand, the trajectories from the literature show chaotic behaviors, suggesting that these are numerical artifacts in their calculations.

Figures 5, 6 and 7 show the trajectories of all the scalar, electromagnetic and gravitational QNMs tabulated in this work, respectively. In all these figures,  $+|m|$  and  $m = 0$  modes are plotted with solid lines, while  $-|m|$  modes are plotted with dashed lines. They are connected at  $a = 0$  where the QNM frequencies do not depend on  $m$ . Trajectories with the same value of  $|m|$  are plotted with the same color.

Note that these plots are intended to help understand general trends and anomalies in those QNM trajectories and inspect our calculations for numerical artifacts. In Sec. IV, we will discuss in-depth some of their features.

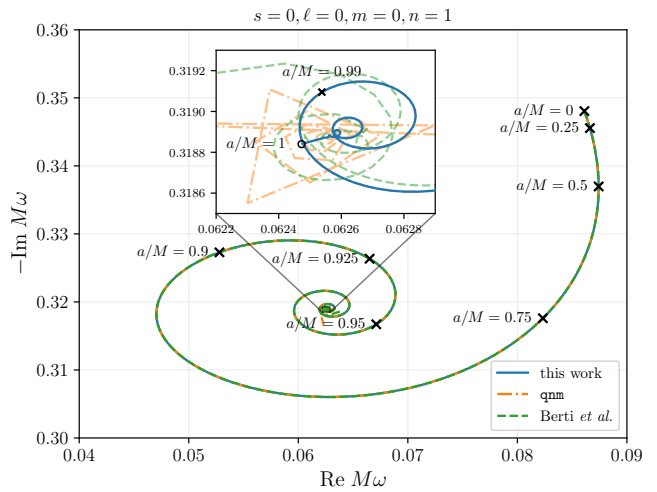


FIG. 4. Trajectory of the  $s = 0, \ell = 0, m = 0$  and  $n = 1$  QNM frequencies. Discrepancies of the frequencies from this work with literature begin only at near-extremal spins where  $a/M \gtrsim 0.99$ . Our trajectory of the QNM (blue solid curve), computed up to  $a/M = 0.9999$ , approaches to the extremal  $a = M$  limit (open circle) found in literature [41].

### C. Quasinormal mode excitation factors

Once the frequency of a QNM is determined, it is straightforward to compute its corresponding QNEF using Eq. (12), as  $A_{\text{in}}$  and  $A_{\text{out}}$  have already been computed during the process. In particular, since  $A_{\text{in}}(\omega)$  is analytic in  $\omega$  [25], therefore  $dA_{\text{in}}/d\omega$  can be computed either along the real or the imaginary axis of  $\omega$ , and both approaches should give the same result. Here, we use a central finite differencing scheme with Richardson extrapolation [42] to estimate the derivative numerically.

QNEFs can be defined with either the Teukolsky amplitudes or the SN amplitudes by using the appropriate  $A_{\text{in, out}}^{\text{T/SN}}$  in Eq. (12). A Teukolsky QNEF  $B_n^{\text{T}}$  and the corresponding SN QNEF  $B_n^{\text{SN}}$  are off by some known frequency-dependent conversion factors where

$$B_n^{\text{T}} = \left( \frac{B_{\text{T}}^{\text{ref}}}{B_{\text{SN}}^{\text{ref}}} \right) \left( \frac{B_{\text{T}}^{\text{inc}}}{B_{\text{SN}}^{\text{inc}}} \right)^{-1} B_n^{\text{SN}}, \quad (36)$$

and the expressions for  $B_{\text{T}}^{\text{ref}}/B_{\text{SN}}^{\text{ref}}$  and  $B_{\text{T}}^{\text{inc}}/B_{\text{SN}}^{\text{inc}}$  can be found in, for example, Ref. [12].

A much-underappreciated fact regarding QNEFs is that perturbations of spin  $s$  and  $-s$  (with  $s \neq 0$ ) have *different* QNEFs despite sharing the same frequency spectrum. This can be seen from the Teukolsky-Starobinsky identities [38, 39] mentioned earlier in the text. For  $s = \pm 2$ , we have

$$B_n^{\text{T},(+2)} = \frac{|C|^2}{256\omega^8} B_n^{\text{T},(-2)}, \quad (37)$$

where  $B_n^{\text{T},(\pm 2)}$  refers to the Teukolsky QNEF for  $s = \pm 2$ , respectively, and that the expression for  $|C|^2$  can be found

<sup>11</sup> Except for  $s = \ell = m = 0$ , where we only tabulate the  $n = 0, 1$  modes.

## scalar QNMs

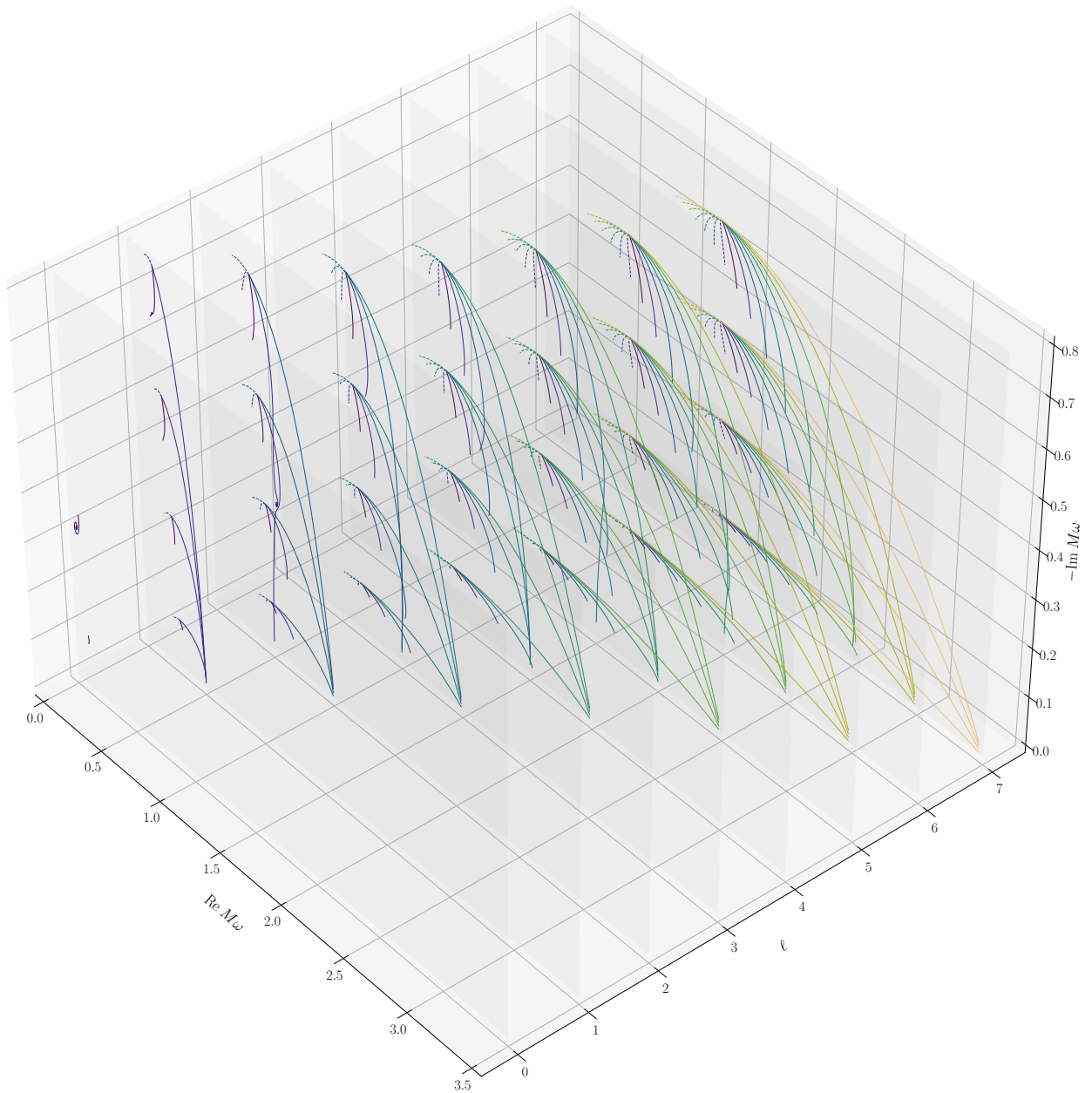


FIG. 5. Trajectories of scalar ( $s = 0$ ) QNMs tabulated in this work ( $-\ell \leq m \leq \ell$  for  $0 \leq \ell \leq 7$ ) parametrized by  $a/M \in [0, 1 - 10^{-4}]$ , up to their third overtones (i.e.,  $n \leq 3$ ), except for the  $s = \ell = m = 0$  mode. Modes with  $m \geq 0$  are plotted with solid lines, while  $m < 0$  modes are plotted with dashed lines. In addition, modes with the same value of  $|m|$  are plotted with the same color and connected at  $a/M = 0$ , and the value of  $a/M$  increases away from that connection point. Another set of QNMs can be obtained by simply “mirroring” the modes shown here along the imaginary  $M\omega$  axis and thus not plotted explicitly. Note that this plot is intended to look for general trends and anomalies in those QNM trajectories and inspect our calculations for numerical artifacts. Numerical values of these QNM frequencies are available online – see [Data Availability](#).

## electromagnetic QNMs

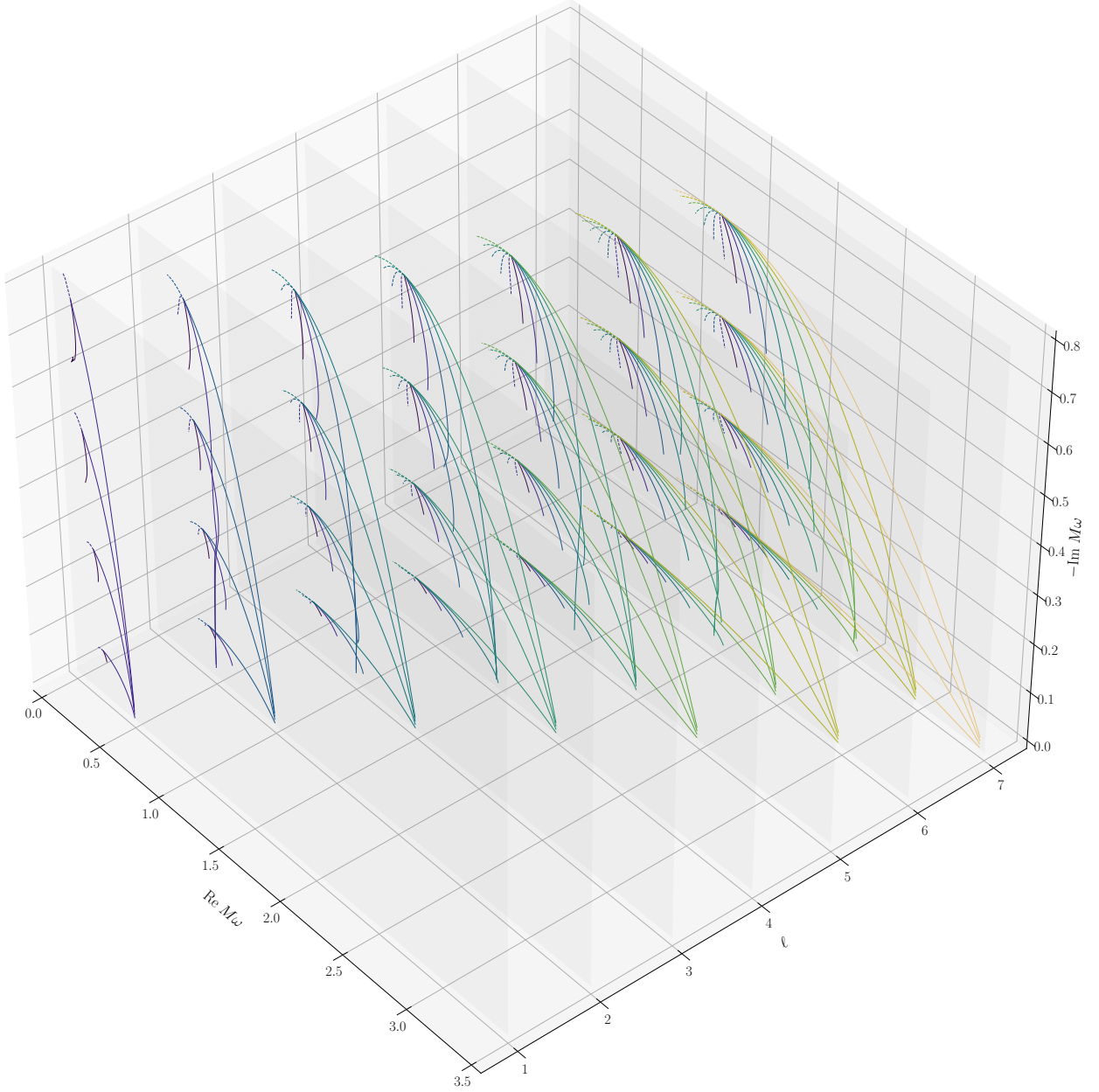


FIG. 6. Same as Fig. 5, but for electromagnetic ( $s = \pm 1$ ) QNMs tabulated in this work ( $-\ell \leq m \leq \ell$  for  $0 \leq \ell \leq 7$ ), up to their third overtones (i.e.,  $n \leq 3$ ). Numerical values of these QNM frequencies are available online – see [Data Availability](#).

## gravitational QNMs

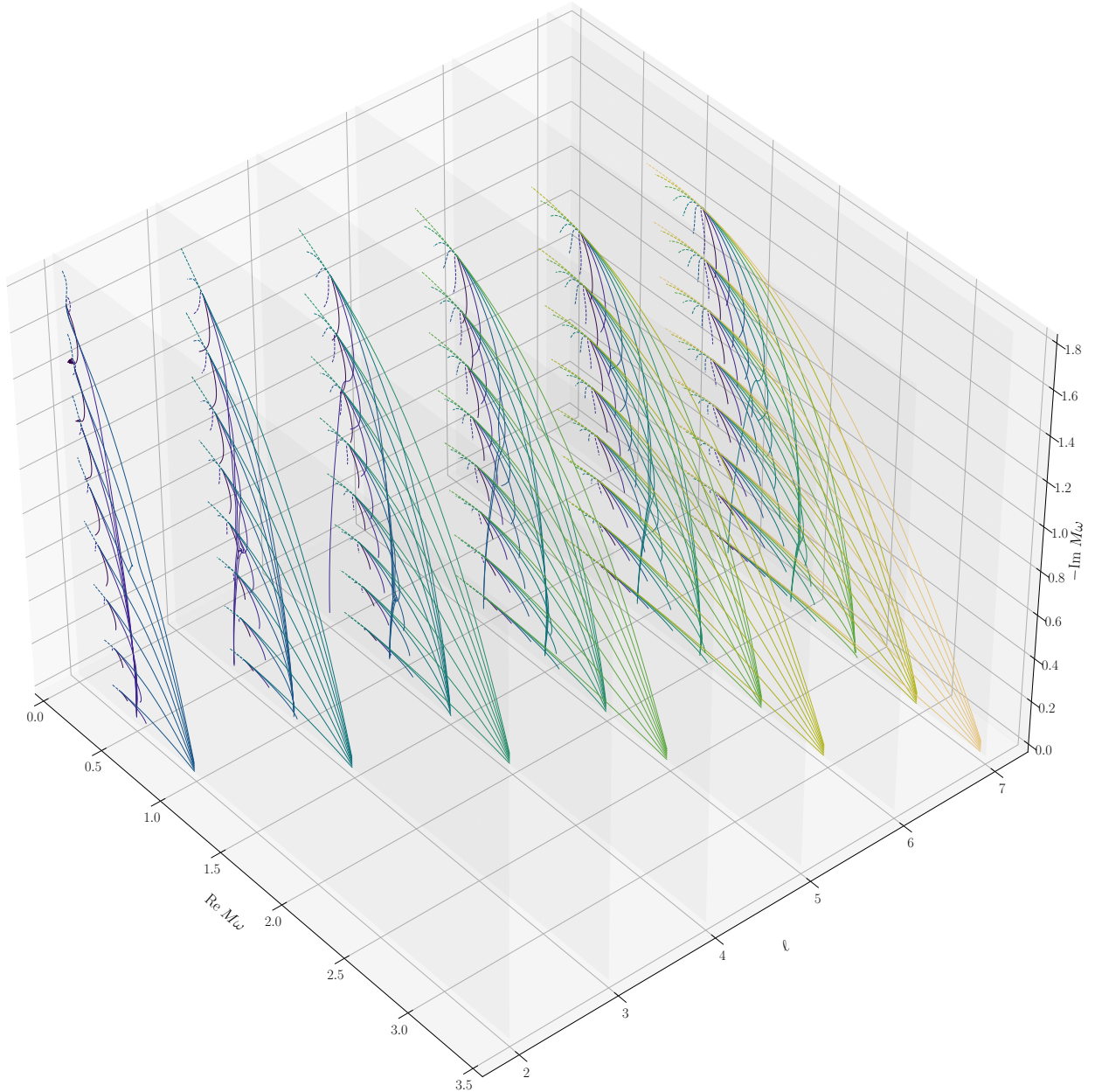


FIG. 7. Same as Fig. 5, but for gravitational ( $s = \pm 2$ ) QNMs tabulated in this work ( $-\ell \leq m \leq \ell$  for  $0 \leq \ell \leq 7$ ), up to their seventh overtones (i.e.,  $n \leq 7$ ). Numerical values of these QNM frequencies are available online – see [Data Availability](#).

in Ref. [39]. Despite what the notation might suggest,  $|\mathcal{C}|^2$  can actually be complex [43]. Similarly for  $s = \pm 1$ , we have

$$B_n^{\text{T},(+1)} = \frac{\mathcal{B}^2}{16\omega^4} B_n^{\text{T},(-1)}, \quad (38)$$

where the expression for  $\mathcal{B}^2$  can again be found in Ref. [39].

Here, we tabulate the QNEFs for the QNMs shown in Sec. III B. In this work, we compute  $B_n^{(\pm s)}$  explicitly and do not use Eqs. (37) and (38) to obtain  $B_n^{(+s)}$  from  $B_n^{(-s)}$  and vice versa. This is because the conversion factors involve large powers of  $\omega$  (more concretely,  $\omega^8$  for  $s = \pm 2$  and  $\omega^4$  for  $s = \pm 1$ ), and thus, the numerical values of  $\omega$  need to be determined to higher precision in order to convert  $B_n^{(\pm s)}$  from  $B_n^{(\mp s)}$  computed numerically. Moreover, we only tabulate the QNEFs for “ordinary modes” ( $\omega_{s\ell mn}^+$ , where the real part of the frequencies are positive), and the QNEFs for mirror modes  $\omega_{s\ell mn}^-$  are related to their ordinary mode counterparts simply by a complex conjugation because of Eq. (35), i.e.,

$$B_n|_{\omega=\omega_{s\ell mn}^-} = B_n|_{\omega=\omega_{s\ell(-m)n}^+}^*. \quad (39)$$

These tables are available online, and a gallery of plots showing the trajectories of the mode frequency and the corresponding QNEF for all the QNMs tabulated in this work can be found online – see [Data Availability](#).

It is again important to note that most of the QNEFs tabulated in this work have been previously computed. As an example, Table I shows a few gravitational ( $s = \pm 2$ ) QNEFs from this work and Motohashi [22, 44], respectively. The two works agree while using completely different and independent approaches. Note that Refs. [22, 44] use a convention  $M = 1/2$  instead of  $M = 1$ . The scaling with  $M$  for Teukolsky QNEFs is nontrivial and  $s$ -dependent. In fact, the combination  $M^{-2s} B_n^{\text{T},(s)}$  gives the dimensionless Teukolsky QNEFs, while SN QNEFs are trivially dimensionless.<sup>12</sup> For example, one would need to divide the values for the gravitational QNEFs from Refs. [22, 44] by 16 to convert to the  $M = 1$  convention properly.

However, we both disagree with earlier literature such as Ref. [18] and Ref. [20]. Other than the fact that Ref. [18] did not make the distinction between Teukolsky QNEFs and SN QNEFs, our discrepancies can be traced back to an ambiguity in the definition of the tortoise coordinate where there is a freedom to choose the integration constant while solving Eq. (15). The community has canonically chosen a particular integration

constant such that  $r_*(r)$  is given by Eq. (6). Note that this degree of freedom is equivalent to the one that allows us to choose the matching point  $r_*^{\text{mp}}$  [cf. Eq. (16)] where choosing  $r_*^{\text{mp}} = 0$  is identical to choosing the integration constant like Eq. (6). Explicitly, if we denote a QNEF computed with  $r_*^{\text{mp}} = k$  as  $B_n|_{r_*^{\text{mp}}=k}$ , then

$$B_n|_{r_*^{\text{mp}}=0} = B_n|_{r_*^{\text{mp}}=k} e^{-2ik\omega_n}. \quad (40)$$

This degeneracy was also noted in Ref. [45] in a different context. It is, therefore, essential to keep track of the choice(s)<sup>13</sup> made for this constant shift in the tortoise coordinate.

In Table I, again as an example, we show some of the values for both  $B_n^{\text{T},(+2)}$ , which are for the first time computed explicitly, and  $B_n^{\text{T},(-2)}$ . They are in excellent agreement with Eq. (37). We have also compared our values, though not shown here, from our explicit calculations for  $B_n^{\text{T},(+1)}$  with that converted from  $B_n^{\text{T},(-1)}$  using Eq. (38) and also find excellent agreement.

## IV. DISCUSSION OF RESULTS

### A. Behavior of quasinormal mode trajectories in the complex plane

From Figs. 5, 6 and 7, we can look for patterns in scalar, electromagnetic and gravitational QNM frequencies, respectively. We see that for most of the  $m \geq 0$  “ordinary” QNMs (solid lines), their real part of the frequencies increase monotonically from  $a = 0$  to their maximal values as  $a \rightarrow 1$ , while their imaginary part of the frequencies become less negative (i.e., longer damping times  $\tau \equiv -1/\text{Im } \omega$ ), also monotonically. Though there are some notable exceptions to this, which will be discussed later in Sec. IV A 2. For  $m < 0$  ordinary modes, the trajectories are tangent to their positive  $m$  counterparts at  $a = 0$ . Their trends with increasing  $a$  are, however, less obvious. Usually for  $m = -\ell$  modes, the real part of the frequencies become smaller and the imaginary part of the frequencies become more negative (i.e., shorter damping times) with increasing  $a$ , while for modes with lower  $|m|$ , the trends are completely opposite.

#### 1. Quasinormal mode trajectories when approaching the extremal Kerr limit

Most of the QNMs with  $\ell = |m| (\neq 0)$ <sup>14</sup> tend to accumulate at  $\omega_n = m/2$  when  $a \rightarrow 1$ , again, with some

<sup>12</sup> This is because the amplitudes for the purely ingoing and the purely outgoing part of the Teukolsky solution  $R_{\text{in}}(r \rightarrow \infty)$  near infinity, i.e.,  $u_{\text{in}}^\infty$  and  $u_{\text{out}}^\infty$  in Eq. (4), respectively, scale differently with  $r$  depending on the value of  $s$ , while those for the SN solution  $X_{\text{in}}(r \rightarrow \infty)$  do not scale with  $r$  at all.

<sup>13</sup> This “constant” can be chosen differently depending on the value of  $\omega_n$  so long as it is accounted for. In fact, we leverage this freedom to gain efficiency in computations (see Appendix A).

<sup>14</sup> Recall that there is another set of QNM frequencies (mirror modes) with  $\{\omega_{s\ell mn}^- \equiv -\omega_{s\ell(-m)n}^+\}$  that are not shown explicitly in Figs. 5, 6 and 7.

TABLE I. A table of a few gravitational QNEFs, rounded to the nearest sixth decimal place. The full tables for scalar, electromagnetic and gravitational QNEFs are available online – see [Data Availability](#).

$\ell$	$m$	$n$	$a/M$	$M = 1$	$M = 1/2$	$M = 1$
				$B_n^{\text{T},(-2)}$ (this work)	$1/16 \times (B_n^{\text{T},(-2)}$ from Refs. [22, 44])	$B_n^{\text{T},(+2)}$ (this work)
2	2	0	0	$0.001599 - 0.001055i$	$0.001599 - 0.001055i$	$2.778095 + 8.976020i$
			0.7	$0.002967 + 0.010638i$	$0.002967 + 0.010638i$	$-1.268880 + 0.786292i$
			0.9999	$0.000124 + 0.005321i$	$0.000124 + 0.005321i$	$-0.000005 + 0.004066i$
3	3	1	0	$0.006990 + 0.002490i$	$0.006990 + 0.002490i$	$-9.537232 - 9.735256i$
			0.7	$-0.088686 + 0.005499i$	$-0.088686 + 0.005499i$	$3.791563 - 2.194855i$
			0.9999	$-0.000594 - 0.047323i$	$-0.000594 - 0.047323i$	$0.000361 - 0.006627i$

exceptions (e.g.,  $|s| = \ell = m = 2, n = 5$ ). This is however not limited only to  $\ell = |m|$  modes. For example, it can also be seen in the  $|s| = 2, \ell = 7, m = 6$  trajectory in Fig. 7. As noted in Refs. [46] and [47] and clearly visible in Figs. 5, 6 and 7, there are two limiting behaviors or branches for the QNMs when  $a \rightarrow 1$ , namely zero-damping modes where  $\text{Im } \omega_n \rightarrow 0$  and thus infinite damping times, and damped modes where  $\text{Im } \omega_n \not\rightarrow 0$ .

While very tempting, we are not able to distinguish if a particular QNM is a zero-damping one or a damped one since our calculations are only up to  $a = 1 - 10^{-4}$  and not exactly at  $a = 1$ . However, given that  $\omega_n$  should be a smooth function of  $a$ , the QNM frequency computed sufficiently close to  $a = 1$  should be indicative [41]. Therefore, if the limiting value for the imaginary part of a QNM frequency is clearly away from 0 (e.g., the  $s = \ell = m = 0, n = 1$  mode as shown in Fig. 4), we can still confirm that a QNM is a damped mode with our results.

## 2. Crossings of quasinormal mode trajectories

Some of the QNM trajectories, however, show rather peculiar features as shown in Figs. 5, 6 and 7 and deviate from the general trends described earlier in this section. For instance, the  $s = \ell = m = 0, n = 1$  QNM trajectory in Fig. 4 exhibits a spiraling motion in the complex frequency plane as  $a$  approaches extremality forming multiple knots before settling down to the  $a = 1$  limit, away from the real axis. This example is by no means isolated. In fact, there are many more modes (that are tabulated in this work) that show similar behaviors (e.g.,  $|s| = 2, \ell = 2, m = 0, n = 5, 6, 7$ , to just name a few).

Another notable example includes the  $|s| = \ell = m = 2, n = 5$  mode, which also forms a knot in the complex frequency plane and converges to a frequency with nonzero imaginary part at  $a = 1$ . This particular mode received considerably more interest (e.g., Refs. [21, 22, 31]) because of its observational relevance by GW detectors. It was recently remarked in a footnote of Ref. [48] and further explored by Ref. [22] that the phenomenon of eigenvalue repulsion can explain this peculiarity.

Avoided crossing is well understood in the context of quantum mechanics (see, for example, Refs. [27, 49]). The real eigenvalues (corresponding to physical observables) of a quantum system described by a Hermitian Hamiltonian with  $k$ -many real parameters avoid crossing and repel from each other, except when the system has a degeneracy or on a  $(k - 2)$  dimensional manifold [49]. In literature, this phenomenon goes by different names, including eigenvalue repulsion, level crossing, etc, that carry the same meaning in the Hermitian case.

For non-Hermitian systems, however, their eigenvalues can be complex. In particular, the real part of a complex eigenvalue is referred to as the (energy) level, while the imaginary part is referred to as the width since the corresponding eigenfunction decays spatially. These systems also exhibit eigenvalue repulsion. However, the real part (i.e., the levels) or the imaginary part (i.e., the widths) of the eigenvalues can cross each other but *not simultaneously*. Unique to non-Hermitian systems is that when two levels cross each other, the corresponding widths repel, and vice versa [50].

Let us consider a simple two-level system where the (effective) Hamiltonian  $H_{\text{eff}}$  is given by [50, 51]

$$H_{\text{eff}} = \begin{pmatrix} \epsilon_1 & 0 \\ 0 & \epsilon_2 \end{pmatrix} + \lambda \begin{pmatrix} V_{11} & V_{12} \\ V_{21} & V_{22} \end{pmatrix}, \quad (41)$$

where  $V_{ij}, \epsilon_{1,2} \in \mathbb{C}$  are constants and  $\lambda \in \mathbb{C}$  is a “control parameter” that in general can be complex, though it is usually restricted to be real for physical systems. The eigenvalues  $E_{1,2}$  under this model is thus given by

$$E_{1,2} = \frac{1}{2} \left\{ \lambda (V_{11} + V_{22}) + (\epsilon_1 + \epsilon_2) \mp \sqrt{4\lambda^2 V_{12} V_{21} + [\lambda (V_{11} - V_{22}) + (\epsilon_1 - \epsilon_2)]^2} \right\}. \quad (42)$$

When  $\lambda$  is allowed to be complex, the Hamiltonian can be thought of as having two real parameters  $\text{Re } \lambda$  and  $\text{Im } \lambda$ , respectively. This means that the two eigenvalues can now cross on a 0 dimensional manifold (i.e., discrete disconnected points), referred to as exceptional points in literature [51, 52]. For this two-level system, the eigenvalues cross when the expression inside the square root

in Eq. (42) vanishes. This means that the exceptional points  $\lambda_{\text{EP}}$  of this model are located at

$$\lambda_{\text{EP}} = \frac{-(\epsilon_1 - \epsilon_2)(V_{11} - V_{22}) \pm 2i(\epsilon_1 - \epsilon_2)\sqrt{V_{12}V_{21}}}{4V_{12}V_{21} + (V_{11} - V_{22})^2}. \quad (43)$$

In fact, the two eigenvalues  $E_{1,2}(\lambda \in \mathbb{C})$  can be visualized as two Riemann surfaces that intersect at  $\lambda = \lambda_{\text{EP}}$ . Importantly, these Riemann surfaces *smoothly* connect different branches of the multivalued square root function in Eq. (42) across its branch points, which exactly correspond to the exceptional points. This is illustrated in Fig. 8, where we plot  $\text{Re } E_{1,2}(\lambda \in \mathbb{C})$  (left panel) and  $\text{Im } E_{1,2}(\lambda \in \mathbb{C})$  (right panel) as two surfaces, separately and respectively. In this example, one of the branch points/exceptional points is located at around  $\lambda_{\text{EP}} \approx 0.52 + 0.62i$  (indicated by a cross). Following the upper surface in the right panel of Fig. 8 that corresponds to  $E_1$  from the left to the right across the branch point, one needs to choose the branch that has an opposite sign to the branch chosen left to the branch point to ensure continuity (and vice versa for the lower surface for  $E_2$ ). This is the mathematical origin of eigenvalue repulsion, stemming from the continuity of the eigenvalues in the control parameter  $\lambda$ . The real part of the eigenvalues  $\text{Re } E_{1,2}$  as shown in the left panel of Fig. 8 cross each other around the branch point with the properly chosen branches. It had also been demonstrated that the same intuition holds even when there are more than two levels in a system [50].

In the context of BHs, the linear differential operators associated with their (linear) perturbations are non-Hermitian, also evident from the fact that their QNM frequencies are complex. Eigenvalue repulsion has been reported in the QNM spectra of charged rotating BHs [48], as well as rotating BHs coupled with a massive scalar field of mass  $\mu$  [53]. In both cases, the spectra are parametrized by two real parameters. Moreover, in the later case, an exceptional point located at real values of  $a$  and  $\mu$  was found for the first time [53]. The reality of the exceptional point has implications beyond simply confirming the mathematical model of avoided crossing. Physically, this leads to hysteresis where the state of a BH depends on the path that it has taken around such an exceptional point, which can be realized by a series of physical processes such as varying the angular momentum of the BH and the mass of the scalar field.

From our discussions, we can see that eigenvalue repulsion is a generic feature ubiquitous in eigensystems. It originates from branch point singularities and has little to do with the nature of gravity. Here, we analyze two examples of the crossing of the real or the imaginary part of the QNM trajectories (but not simultaneously) using the mathematical theory of eigenvalue repulsion.

The first example that we consider is the  $s = \pm 1, \ell = 2, m = 1$  mode. The real part of the QNM frequency of the  $n = 2, 3$  overtones cross each other at around  $a \approx 0.9785$  (see the blue and orange solid curves in Fig. 9a,

respectively). The imaginary part of the frequencies can be seen to repel each other slightly at around the same value of  $a$  in Fig. 9b. As a first attempt, we fit the complex QNM frequencies *locally* around this crossing point (from  $a_0 = 0.975$  to  $a_1 = 0.982$ , for a total of 142 complex frequencies) with the two-level effective Hamiltonian in Eq. (41) where its eigenvalues  $E_{1,2}$  model the complex QNM frequencies, i.e.,  $E_{1,2} \equiv \omega_{1,2}$ .<sup>15</sup> The control parameter  $\lambda$  in this case is simply  $a$  rescaled such that it is bounded between  $\lambda \in [0, 1]$ , i.e.,  $\lambda \equiv (a - a_0)/(a_1 - a_0)$ . Note that there are only 10 real variables to be fitted (instead of 12) in this phenomenological model. This is because as far as eigenvalues are concerned,  $V_{12}$  and  $V_{21}$  enter only as the product  $V_{12}V_{21}$  in Eq. (42). In fact, we will set  $V_{12} = V_{21}$  without loss of generality hereinafter.

The best-fit results for the two overtones are shown as the dashed curves in Figs. 9a and 9b, respectively. We see that the phenomenological model fits the QNM frequency data very well, reproducing the crossing in the real part of the frequencies and the repulsion in the imaginary part of the frequencies with just 10 degrees of freedom.<sup>16</sup> Note that the model needs to fit simultaneously the real and the imaginary part of both QNMs. Therefore, the excellent agreement of the fit with the data is unlike to be due to overfitting. From the model, we can also infer that there are two exceptional points in the complex- $a$  parameter space at roughly  $a_{\text{EP}}^{(1)} \approx 0.979 - 0.024i$  with  $\omega_{\text{EP}}^{(1)} \approx 0.654 - 0.275i$  and  $a_{\text{EP}}^{(2)} \approx 0.979 + 0.004i$  with  $\omega_{\text{EP}}^{(2)} \approx 0.527 - 0.297i$ , respectively. Unlike Ref. [53], these exceptional points *cannot* be encircled via physical processes (i.e., spinning a BH up or down) and thus not physically interesting. That said, their mathematical existence still influences the QNM trajectories as shown here, and can be confirmed by analytically continuing the Teukolsky solutions for a complex value of  $a$ . We leave this for future work.

To demonstrate that the agreement is not just accidental, we repeat the exercise with another example, the  $|s| = \ell = m = 2$  and  $n = 5, 6$  modes. This time we fit the QNMs with the two-level effective Hamiltonian using even more data from  $a_0 = 0.89$  to  $a_1 = 0.93$  for a total of 622 complex frequencies. The best-fit results are shown as the dashed curves in Figs. 10a and 10b, respectively. Once again, the model fits the data very well (solid curves in both figures) and reproduces the crossing

<sup>15</sup> One could have also chosen the eigenvalues as  $E_{1,2} = (\omega_{1,2})^2$  instead, as one can recast the GSN equation into a form that resembles the Schrödinger equation, i.e.,  $d^2Y/dr_*^2 + [\omega^2 - V_Y(r_*)]Y = 0$ , where  $Y \equiv X/\sqrt{\eta}$  (note that  $\eta$  is frequency dependent) and  $V_Y$  can be expressed in terms of  $\mathcal{F}$  and  $\mathcal{U}$  [12]. Since we do not attempt to map the two-level model back into the GSN equation, both choices are valid and we chose  $E_{1,2} = \omega_{1,2}$  for ease of demonstration.

<sup>16</sup> One could even argue that there are effectively only 6 degrees of freedom instead, since  $\epsilon_{1,2} \in \mathbb{C}$  can be read off or determined simply from the  $a = a_0$  values.

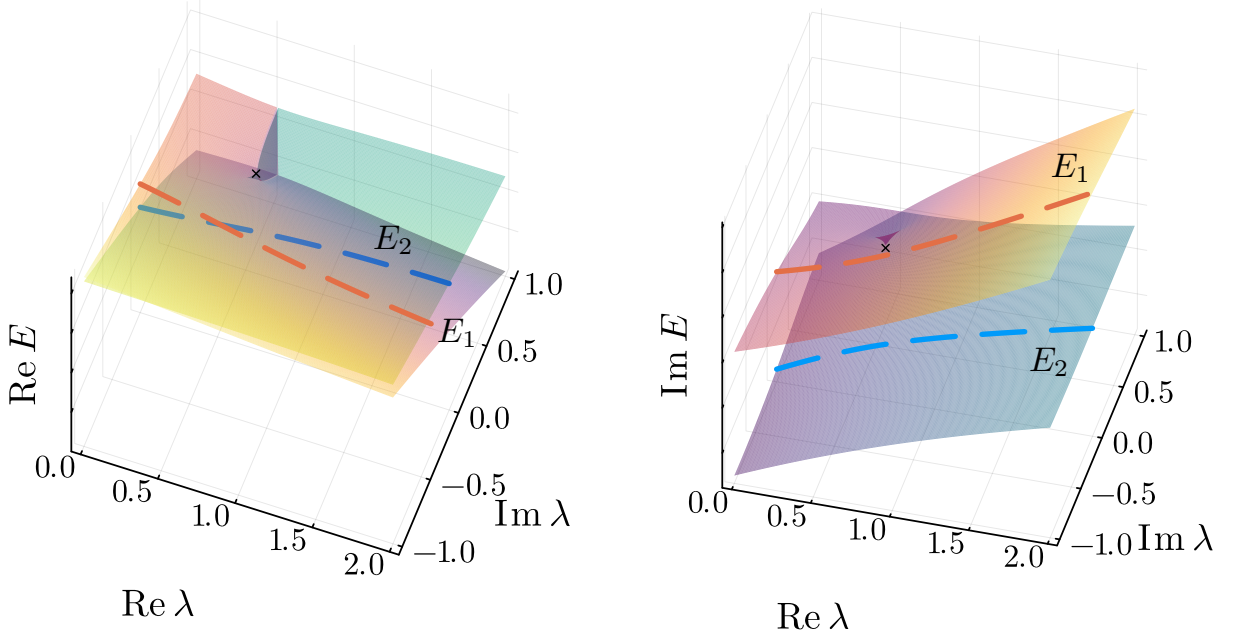


FIG. 8. Two eigenvalues  $E_{1,2}(\lambda \in \mathbb{C})$  visualized as two Riemann surfaces that intersect at exceptional points (left panel: the real part, right panel: the imaginary part). In this example, one of the exceptional points is located at around  $\lambda_{\text{EP}} \approx 0.52 + 0.62i$ , which is indicated by a cross. The dashed lines correspond to the two physically relevant slices  $E_{1,2}(\lambda \in \mathbb{R})$  along  $\text{Im } \lambda = 0$ .

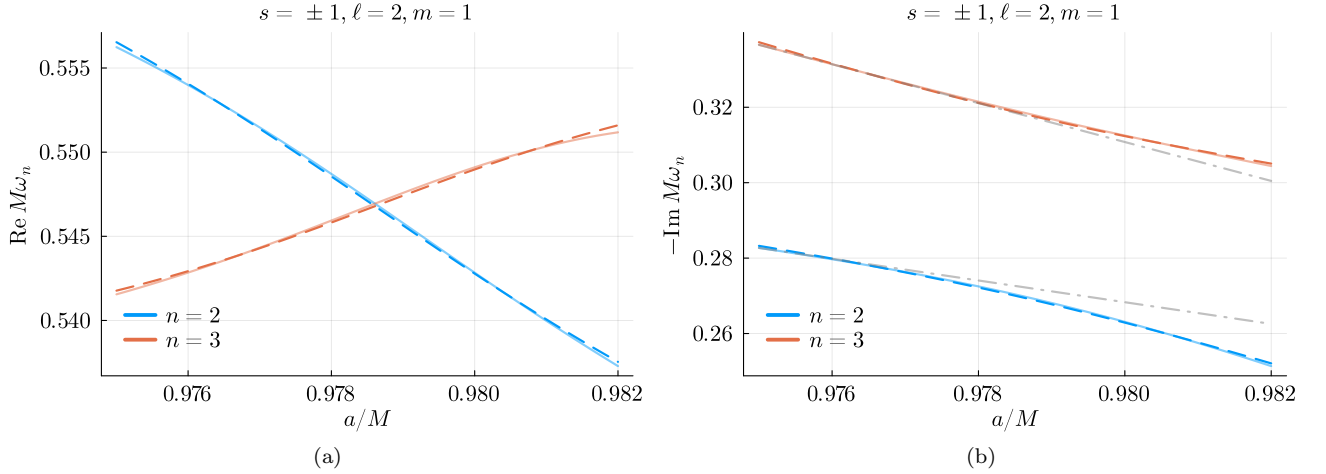


FIG. 9. Real and imaginary part of the QNM frequencies of the  $s = \pm 1, \ell = 2, m = 1$  with  $n = 5$  and  $n = 6$  from  $a/M = 0.975$  to  $a/M = 0.982$ , respectively. The solid curves on both panels show the actual values for the frequencies, while the dashed curves show the best-fit results using the two-level effective Hamiltonian in Eq. (41). With only 10 degrees of freedom, the model reproduces the crossing in the real part of the frequencies and the corresponding repulsion in the imaginary part of the frequencies. The dashdot lines on the right panel are the tangents of the curves at  $a/M = 0.975$  to contrast the repulsion among the two overtones more clearly.

in the imaginary part of the frequencies and the corresponding repulsion in the real part of the frequencies with only a few degrees of freedom. Using the model, we infer that there are two exceptional points in the complex- $a$  parameter space at roughly  $a_{\text{EP}}^{(1)} \approx 0.897 + 0.010i$  with

$\omega_{\text{EP}}^{(1)} \approx 0.550 - 0.755i$  and  $a_{\text{EP}}^{(2)} \approx 0.876 + 0.032i$  with  $\omega_{\text{EP}}^{(2)} \approx 0.490 - 0.772i$ , respectively. Despite being able to easily explain the QNM trajectories near the point where the real/imaginary part of the frequencies cross, we want to caution with the caveats that the two-level model does

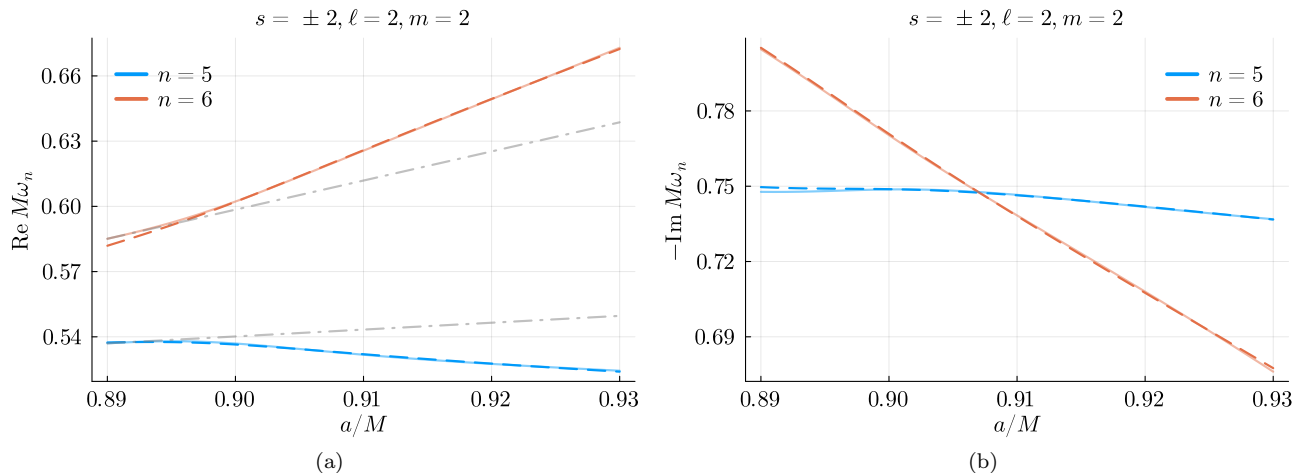


FIG. 10. Same as Fig. 9 but for  $|s| = \ell = m = 2$  and  $n = 5, 6$  QNEFs.

not take into account interactions from other overtones (in fact, the  $n = 5$  overtone crosses both  $n = 6$  and  $n = 7$  overtones but at different values of  $a$ ) and that the model is only a local expansion of the much more complicated eigensystem.

### 3. Resonant excitation of quasinormal modes

Most of the QNEF trajectories, parametrized by  $a$ , computed in this work are either in a spiral motion (also noted in Ref. [22]) or in a parabolic/hyperbolic-like motion in the complex plane as  $a$  increases from 0 to 0.9999. However, like the QNM trajectories, some of the QNEF trajectories show anomalous features.

For instance, Fig. 11 shows the QNM (left panel) and the QNEF (right panel) trajectories for the  $s = -2, \ell = m = 2$  and  $n = 5, 6$  modes. The two QNEF trajectories, as first pointed out in Ref. [22], spiral against each other in a lemniscate-like pattern (also known as a “figure-8” pattern) near the value of  $a \approx 0.897$  where the  $n = 5$  QNM trajectory forms a knot. As shown explicitly in Sec. IV A 2, this is related to eigenvalue repulsion near exceptional points.

Figure 12 shows another example for electromagnetic QNMs with  $s = -1, \ell = 2, m = 1$  and  $n = 2, 3$ . Similar to Fig. 11, these two modes show eigenvalue repulsion as demonstrated in Sec. IV A 2. However, unlike Fig. 11, we do not see a complete lemniscate in the QNEF trajectories that Ref. [22] suggests to signify the occurrence of a resonant excitation near exceptional points. This is likely due to the fact that the two exceptional points as inferred by the two-level effective Hamiltonian model are further away from the QNM trajectories compared to the gravitational case shown in Fig. 11, and thus are amplified to a lesser extent.

## B. Comparisons with other methods

Besides the method presented here, there are other techniques for computing QNM frequencies and QNEFs of Kerr BHs, each with their strengths and weaknesses. Here, we outline a few of those and compare them with our method.

Continued-fraction-based methods (e.g., Refs. [30, 32]) write solutions to the Teukolsky equation using a (truncated) finite number of basis functions. The boundary conditions for QNMs are imposed directly to find a recurrence relation, which is solved efficiently by transforming it into a continued fraction equation. As a result, these methods converge very quickly and can produce high-precision QNM frequencies (for one such numerical implementation, see Ref. [40]). However, they are incapable of computing QNEFs.

MST-based methods (e.g. Refs. [20, 22, 54]), on the other hand, leverages the analytic expressions for  $B^{\text{inc, ref}}(\omega)$  [or equivalently  $A_{\text{in, out}}(\omega)$ ] that one can easily evaluate given the values of  $s, \ell, m, a$ , respectively. They are very similar to our method as QNM frequencies are also found by numerically solving a nonlinear equation  $A_{\text{in}}(\omega) = 0$ . However, in our method, the left-hand side of the nonlinear equation,  $A_{\text{in}}(\omega)$ , itself is obtained by numerically integrating the GSN equation. These techniques can compute QNEFs quickly since the asymptotic amplitudes are given as analytical expressions in terms of  $\omega$ . However, the MST method is a highly specialized and specific technique devised for Kerr BHs, and extending the method to other backgrounds might be nontrivial.

Recently, isomonodromic and gauge-theory-inspired methods (e.g., Refs. [47, 55, 56]) have been proposed. They provide an exact quantization rule for QNMs that one can solve directly for a given overtone number  $n$  (though that might not match our convention for labeling overtones) instead of searching for it. Exact expressions

$$s = -2, \ell = 2, m = 2$$

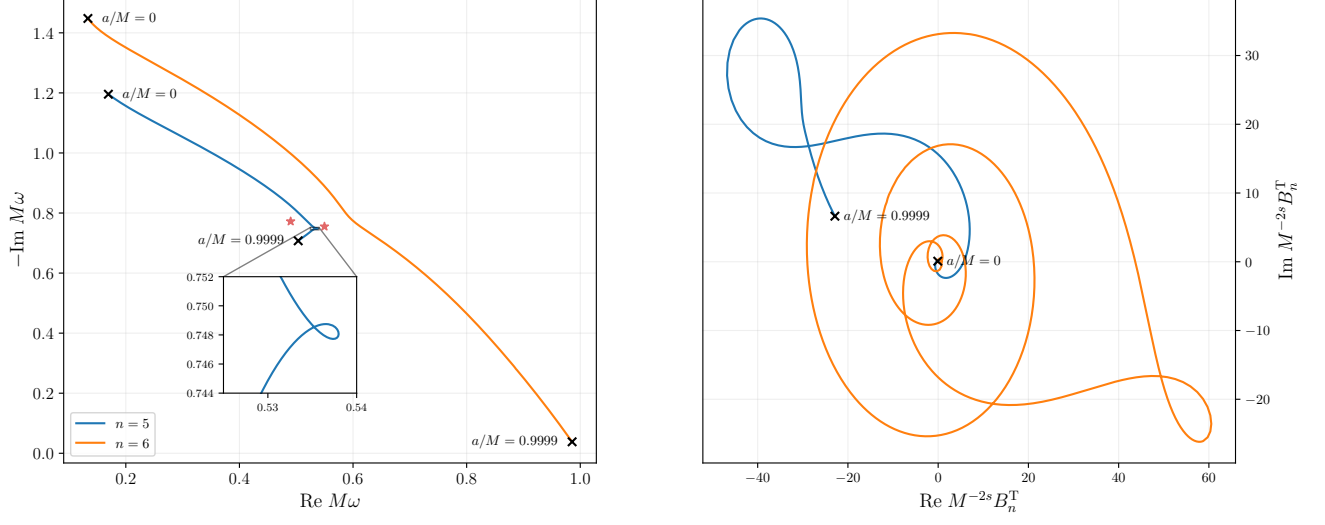


FIG. 11. QNM (left panel) and QNEF (right panel) trajectories, parametrized by  $a/M$ , for the  $s = -2, \ell = m = 2$  and  $n = 5, 6$  modes, respectively. The two frequencies  $\omega_{\text{EP}}$  corresponding to the exceptional points inferred using the two-level model in Sec. IV A 2 are shown by stars in the left panel.

$$s = -1, \ell = 2, m = 1$$

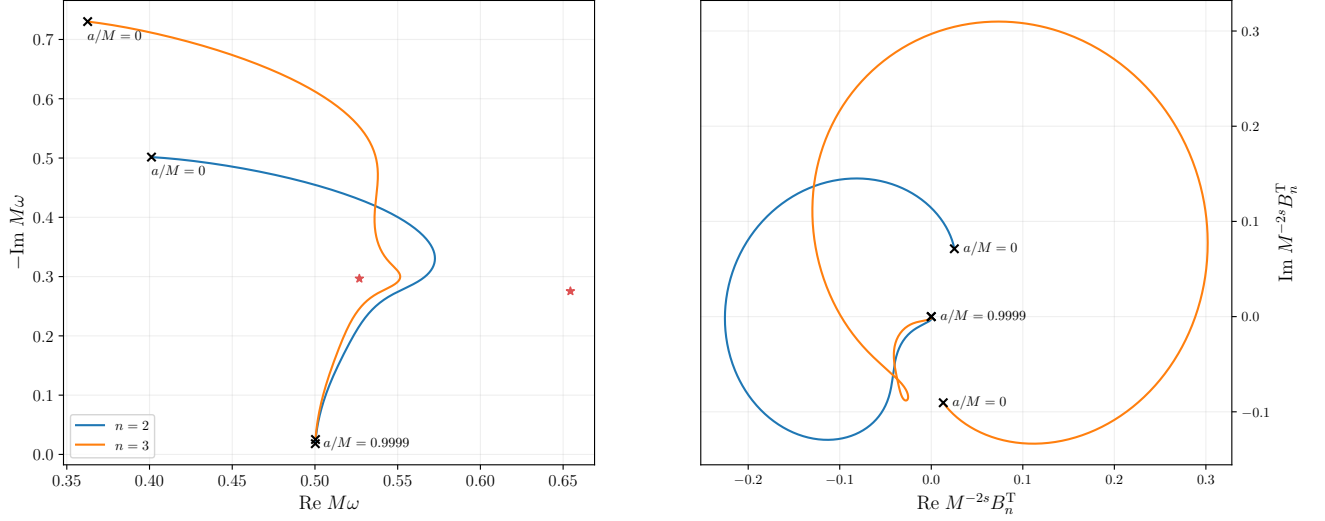


FIG. 12. Same as Fig. 11 but with the  $s = -1, \ell = 2, m = 1$  and  $n = 2, 3$  modes, respectively. However, we do not see a complete lemniscate in the QNEF trajectories as proposed by Ref. [22] that signifies the occurrence of a resonant excitation. This is likely due to the greater distance of the QNM trajectories on the left panel with the frequencies corresponding to the exceptional points as shown by the stars compared to the gravitational case in Fig. 11.

for the asymptotic amplitudes are also provided from these techniques. More importantly, they give us a better analytical understanding of the behaviors of QNMs and their QNEFs than numerical explorations like this paper can offer.

Another recent trend in the computational techniques for Kerr BHs is the adaptation of hyperboloidal coordinates (e.g., [28, 57]). Under the hyperboloidal framework, coordinate transformations are performed to elimi-

nate some of the coordinate artifacts associated with the conventional Boyer-Lindquist coordinates. In particular, QNM solutions are regular at the two boundaries. Coupled with a (pseudo)spectral algorithm, one will also have to solve an eigensystem numerically to obtain QNM frequencies. For one such numerical implementation, see Ref. [28]. Our method is conceptually similar where a coordinate transformation [i.e., a complex scaling transformation, cf. Eq. (16)] is performed to get rid of un-

wanted coordinate artifacts near the boundaries.

The complex scaling transformation is also employed in what their authors referred to as the “quick-and-dirty” method [18, 24]. Indeed, our method bears many resemblances to it in many regards. The key ingredient in such a scheme, as demonstrated in this paper, is really just the complex scaling transformation, and there is no need to use the Prüfer phase transformation. In addition, the matching point for the transformation needs to be chosen carefully and accounted for when comparing with other techniques of computing QNEFs since their values depend on the definition of  $r_*$  [cf. Eq. (40)]. With these improvements, as well as the switch to solving the GSN equation numerically instead of using the phase integral method, we show that one can reliably push the calculations all the way to near extremal rotation (in this work, to  $a = 1 - 10^{-4}$  systematically) and moderate overtones (in this work, up to  $n \leq 7$ )<sup>17</sup> unlike what was claimed in Ref. [18].

## V. CONCLUSION

In this work, we introduce a novel technique based on the GSN formalism to compute the values of the frequencies and the corresponding QNEFs for scalar, electromagnetic, and gravitational QNMs. Specifically, we analytically continue the tortoise coordinate so that GSN solutions remain finite at the horizon and near spatial infinity.

Our results for the QNM frequencies and their QNEFs, in general, agree with previous calculations that were done with independent methods, and thus crossvalidating values found in literature. Furthermore, we clarify that QNEFs also depend on the sign of the spin weight of the perturbing field  $s$ , and that the QNEFs in the Teukolsky formalism are not dimensionless.

Using our data, we further explore the idea that the eigenvalue repulsion theory can explain some of the anomalous QNM and QNEF trajectories in the complex plane. With a simple two-level effective Hamiltonian, we explicitly demonstrate, using two sets of QNM trajectories as examples, that whenever the real part of the eigenvalues cross, the imaginary part of them repel but never simultaneously for real values of  $a$ , and vice versa. Moreover, we show that the extent of the resonant excitation due to eigenvalue repulsion depends also on the proximity to the exceptional point that causes the repulsion.

The approach here can also be extended straightforwardly to compute QNMs and QNEFs of arbitrary backgrounds that admit a second-order ODE as the master equation governing their perturbations. Given such a master equation, apply an isospectral generalized Dar-

boux transformation [58] if necessary to ensure the potential associated with the ODE is short-ranged. Then, use the complex scaling transformation to obtain a transformed ODE that can be solved easily with conventional numerical methods.

## DATA AVAILABILITY

QNM frequencies and QNEFs tabulated in this work are available as comma-separated values (CSV) files at <https://centra.tecnico.ulisboa.pt/network/grit/files/ringdown/>. Each CSV file contains the data for one  $s\ell mn$  mode, which is labeled in its filename. For example, the file `s-2l3m2n1.dat` contains the data for the  $s = -2, \ell = 3, m = 2, n = 1$  mode. The columns from left to right correspond to  $a/M$ ,  $\text{Re } M\omega_{\ell mn}$ ,  $\text{Im } M\omega_{\ell mn}$ ,  $\text{Re } A_{\ell mn}$ ,  $\text{Im } A_{\ell mn}$ ,  $\text{Re } M^{-2s} B_{\ell mn}^T$ ,  $\text{Im } M^{-2s} B_{\ell mn}^T$ ,  $\text{Re } B_{\ell mn}^{\text{SN}}$ ,  $\text{Im } B_{\ell mn}^{\text{SN}}$ , where  $A_{\ell mn}$  is the angular separation constant for the angular Teukolsky equation.

A gallery of interactive plots showing the trajectories of the mode frequencies and the corresponding excitation factors for all the QNMs tabulated in this work can be found at <https://ricokaloklo.github.io/kerr-qnm-qnef>.

## ACKNOWLEDGMENTS

The Center of Gravity is a Center of Excellence funded by the Danish National Research Foundation under grant No. 184. This work was supported by the research grant no. VIL37766 and no. VIL53101 from Villum Fonden, and the DNR Chair program grant no. DNR162 by the Danish National Research Foundation. This work has received funding from the European Union’s Horizon 2020 research and innovation programme under the Marie Skłodowska-Curie grant agreement No 101131233. The Tycho supercomputer hosted at the SCIENCE HPC center at the University of Copenhagen was used for supporting this work. Additionally, RKLL would like to thank Hayato Motohashi and Naritaka Oshita for their correspondence. LS would like to acknowledge support from the Stefan Rozental og Hanna Kobylinski Rozentals Fond.

### Appendix A: Choosing an appropriate matching point $r_*^{\text{mp}}$

Choosing a different matching point  $r_*^{\text{mp}}$  and rotation angle  $\beta$  generates a different *slice* of the analytic-continued  $r(r_*)$  as a function of a real variable  $\rho$  [cf. Eq. (16)]. In Sec. II B, we give the appropriate value of  $\beta$  to rotate such that a GSN function  $X(\rho)$  still behaves like a plane wave asymptotically (i.e.,  $\rho \rightarrow \pm\infty$ ) even

<sup>17</sup> Although not shown in this paper and not done systematically, we did try computing overtones up to  $n = 20$  and found no issue.

with a complex frequency. In this appendix, we focus on choosing the matching point  $r_*^{\text{mp}}$  appropriately.

A desirable  $r(\rho)$  should map  $\rho \rightarrow -\infty$  to  $r \rightarrow r_+$  and  $\rho \rightarrow +\infty$  to  $|r| \rightarrow \infty$ , respectively, such that Eq. (31) is satisfied. In fact, only certain ranges of the matching point  $r_*^{\text{mp}}$  give a  $r(\rho)$  that has these properties. Figure 13 shows  $r(\rho \leq 0)$  for  $a = 0.99$  and  $\beta \approx -0.4996\pi$  (appropriate for  $m = 2$  and  $\omega \approx 0.8662 - 1.178i$ ) with two different matching points (indicated by the crosses at their corresponding values of  $r_*^{\text{mp}}$  in the complex- $r$  plane),  $r_*^{\text{mp}} = 2$  and  $-2$ , respectively, as an example. We see that if we choose the matching point to be at  $r_*^{\text{mp}} = 2$ , then asymptotically  $|r(\rho \rightarrow -\infty)| \rightarrow \infty$ . If we choose the matching point to be at  $r_*^{\text{mp}} = -2$  instead, then  $r$  approaches to  $r_+$  (indicated by the plus sign) as desired.

These behaviors can be understood qualitatively by realizing that Eq. (19) is an autonomous ODE. The arrows in Fig. 13 indicate  $-dr/d\rho$  at each point and the solutions  $r(\rho)$  follow these arrows. There is a critical point on the real  $r$ -axis (which can be converted to a critical value of  $r_*$ ) where all matching points to its left correspond to counterclockwise trajectories that asymptotically approach an equilibrium point on the real axis where  $dr/d\rho = 0$ , in this case at  $r = r_+$ .

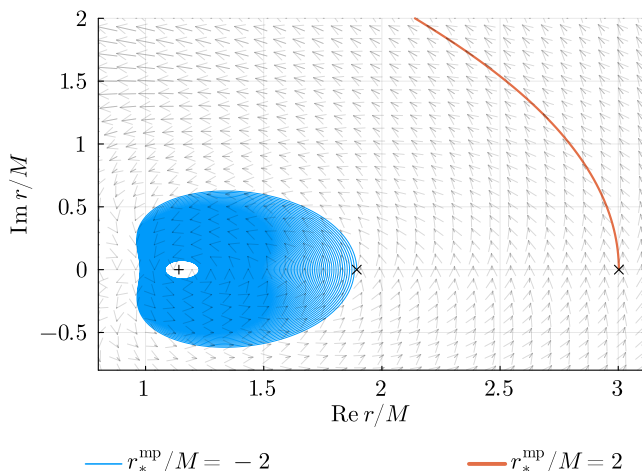


FIG. 13. Two trajectories of  $r(\rho)$  with matching point  $r_*^{\text{mp}} = 2$  and  $-2$ , respectively, as  $\rho$  changes from 0 (crosses) to be more negative.

One might then conclude that the matching point  $r_*^{\text{mp}}$  can be chosen as small and far away from the critical value as one likes. However, we need to consider also the asymptotic behavior of  $r(\rho \rightarrow \infty)$ . Figure 14 shows explicitly two  $r(\rho \geq 0)$  with  $r_*^{\text{mp}} = -2$  and  $-6$ , respectively, for  $\beta \approx 0.2982\pi$ , which is the appropriate value for the same  $a$ ,  $m$  and  $\omega$  assumed in Fig. 13. The arrows in the figure indicate  $dr/d\rho$  at each point such that the solutions  $r(\rho \geq 0)$  follow these arrows. We see that if

the matching point (indicated by a cross) is not chosen correctly, say, at  $r_*^{\text{mp}} = -6$  in this case, then  $r(\rho)$  approaches to an equilibrium point on the real axis (in this case, at  $r = r_-$  as indicated by a dot). On the other hand, with  $r_*^{\text{mp}} = -2$ ,  $r(\rho \rightarrow \infty)$  has the desired trajectory asymptotically as  $\rho \rightarrow \infty$ .

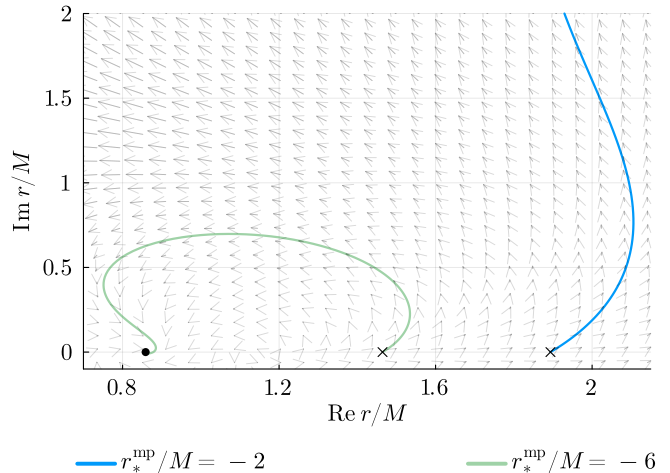


FIG. 14. Two trajectories of  $r(\rho)$  with matching point  $r_*^{\text{mp}} = -2$  and  $-6$ , respectively, as  $\rho$  changes from 0 (crosses) to be more positive.

Similar to the case with  $\rho \leq 0$  as shown in Fig. 13, there is also a critical point in Fig. 14 for the  $\rho \geq 0$  case (which is different since  $\beta$  are not the same) where trajectories starting to the right of the critical point all approach to infinity asymptotically. Therefore, we can set the matching point  $r_*^{\text{mp}}$  anywhere between those two critical points.

Ideally, one would want to choose  $r_*^{\text{mp}}$  as the lower limit of the allowed range such that the corresponding  $r^{\text{mp}}$  in the complex- $r$  plane is closest to the horizon at  $r_+$ . This is because  $r(\rho < 0)$  spirals towards  $r = r_+$  slowly (see, for example, Fig. 13). With a smaller  $r_*^{\text{mp}}$ , the same  $\rho$  corresponds to a value of  $r = r(\rho)$  that is closer (in the modulus sense) to  $r = r_+$ . Therefore, the absolute value of the inner numerical boundary  $|\rho_{\text{in}}|$  needed when solving the GSN equation (cf. Sec. III A) can be smaller and thus it is more efficient.

In practice, however, one needs to evaluate  $e^{\pm i p r_*^{\text{mp}}}$  and  $e^{\pm i \omega r_*^{\text{mp}}}$  during a calculation, which can still be exponentially large or small in modulus. Therefore, one should also make sure that their choice of the matching point  $r_*^{\text{mp}}$  will not make those numbers too big or small. In the numerical implementation `GeneralizedSasakiNakamura.jl`, we enforce that  $1/25 \leq e^{|\text{Im } \omega| |r_*^{\text{mp}}|} \leq 1$  (note that  $\text{Im } \omega = \text{Im } p$ ).

- 
- [1] R. P. Kerr, Gravitational field of a spinning mass as an example of algebraically special metrics, *Phys. Rev. Lett.* **11**, 237 (1963).
- [2] B. P. Abbott *et al.* (LIGO Scientific, Virgo), Observation of Gravitational Waves from a Binary Black Hole Merger, *Phys. Rev. Lett.* **116**, 061102 (2016), [arXiv:1602.03837 \[gr-qc\]](#).
- [3] E. Berti, V. Cardoso, and C. M. Will, On gravitational-wave spectroscopy of massive black holes with the space interferometer LISA, *Phys. Rev. D* **73**, 064030 (2006), [arXiv:gr-qc/0512160](#).
- [4] E. Berti, A. Sesana, E. Barausse, V. Cardoso, and K. Belczynski, Spectroscopy of Kerr black holes with Earth- and space-based interferometers, *Phys. Rev. Lett.* **117**, 101102 (2016), [arXiv:1605.09286 \[gr-qc\]](#).
- [5] E. Berti, V. Cardoso, and A. O. Starinets, Quasinormal modes of black holes and black branes, *Class. Quant. Grav.* **26**, 163001 (2009), [arXiv:0905.2975 \[gr-qc\]](#).
- [6] V. Baibhav, M. H.-Y. Cheung, E. Berti, V. Cardoso, G. Carullo, R. Cotesta, W. Del Pozzo, and F. Duque, Agnostic black hole spectroscopy: Quasinormal mode content of numerical relativity waveforms and limits of validity of linear perturbation theory, *Phys. Rev. D* **108**, 104020 (2023), [arXiv:2302.03050 \[gr-qc\]](#).
- [7] R. H. Boyer and R. W. Lindquist, Maximal analytic extension of the Kerr metric, *J. Math. Phys.* **8**, 265 (1967).
- [8] C. W. Misner, K. S. Thorne, and J. A. Wheeler, *Gravitation* (W. H. Freeman, San Francisco, 1973).
- [9] S. A. Teukolsky, Perturbations of a rotating black hole. 1. Fundamental equations for gravitational electromagnetic and neutrino field perturbations, *Astrophys. J.* **185**, 635 (1973).
- [10] M. Sasaki and T. Nakamura, A class of new perturbation equations for the Kerr geometry, *Physics Letters A* **89**, 68 (1982).
- [11] S. A. Hughes, Computing radiation from Kerr black holes: Generalization of the Sasaki-Nakamura equation, *Phys. Rev. D* **62**, 044029 (2000), [Erratum: *Phys. Rev. D* **67**, 089902 (2003)], [arXiv:gr-qc/0002043](#).
- [12] R. K. L. Lo, Recipes for computing radiation from a Kerr black hole using a generalized Sasaki-Nakamura formalism: Homogeneous solutions, *Phys. Rev. D* **110**, 124070 (2024), [arXiv:2306.16469 \[gr-qc\]](#).
- [13] H. Nakano and N. Sago, *Gravitational Waves and Perturbation Theory*, edited by T. Shiromizu and T. Takayanagi, Research in Theoretical Physics (Asakura Publishing Co., Ltd., Tokyo, Japan, 2022) Chap. 4, ISBN: 978-4-254-13531-2.
- [14] G. B. Arfken, H. J. Weber, and F. E. Harris, Chapter 10 - green's functions, in *Mathematical Methods for Physicists (Seventh Edition)*, edited by G. B. Arfken, H. J. Weber, and F. E. Harris (Academic Press, Boston, 2013) seventh edition ed., pp. 447–467.
- [15] G. B. Arfken, H. J. Weber, and F. E. Harris, Chapter 11 - complex variable theory, in *Mathematical Methods for Physicists (Seventh Edition)*, edited by G. B. Arfken, H. J. Weber, and F. E. Harris (Academic Press, Boston, 2013) seventh edition ed., pp. 469–550.
- [16] E. Berti and V. Cardoso, Quasinormal ringing of Kerr black holes. I. The Excitation factors, *Phys. Rev. D* **74**, 104020 (2006), [arXiv:gr-qc/0605118](#).
- [17] E. W. Leaver, Spectral decomposition of the perturbation response of the Schwarzschild geometry, *Phys. Rev. D* **34**, 384 (1986).
- [18] K. Glampedakis and N. Andersson, Quick and dirty methods for studying black hole resonances, *Class. Quant. Grav.* **20**, 3441 (2003), [arXiv:gr-qc/0304030](#).
- [19] S. R. Dolan and A. C. Ottewill, Wave Propagation and Quasinormal Mode Excitation on Schwarzschild Space-time, *Phys. Rev. D* **84**, 104002 (2011), [arXiv:1106.4318 \[gr-qc\]](#).
- [20] Z. Zhang, E. Berti, and V. Cardoso, Quasinormal ringing of Kerr black holes. II. Excitation by particles falling radially with arbitrary energy, *Phys. Rev. D* **88**, 044018 (2013), [arXiv:1305.4306 \[gr-qc\]](#).
- [21] N. Oshita, Ease of excitation of black hole ringing: Quantifying the importance of overtones by the excitation factors, *Phys. Rev. D* **104**, 124032 (2021), [arXiv:2109.09757 \[gr-qc\]](#).
- [22] H. Motohashi, Resonant excitation of quasinormal modes of black holes, (2024), [arXiv:2407.15191 \[gr-qc\]](#).
- [23] C.-H. Chen, H.-T. Cho, A. Chrysostomou, and A. S. Cornell, A semi-analytic treatment of quasinormal excitation factors in the eikonal regime, (2024), [arXiv:2407.18644 \[gr-qc\]](#).
- [24] H. O. Silva, G. Tambalo, K. Glampedakis, K. Yagi, and J. Steinhoff, Quasinormal modes and their excitation beyond general relativity, *Phys. Rev. D* **110**, 024042 (2024), [arXiv:2404.11110 \[gr-qc\]](#).
- [25] J. B. Hartle and D. C. Wilkins, Analytic properties of the Teukolsky equation, *Communications in Mathematical Physics* **38**, 47 (1974).
- [26] V. De Alfaro and T. Regge, *Potential Scattering* (North-Holland Publishing Company, 1965).
- [27] N. Moiseyev, *Non-Hermitian Quantum Mechanics* (Cambridge University Press, 2011).
- [28] J. L. Ripley, Computing the quasinormal modes and eigenfunctions for the Teukolsky equation using horizon penetrating, hyperboloidally compactified coordinates, *Class. Quant. Grav.* **39**, 145009 (2022), [arXiv:2202.03837 \[gr-qc\]](#).
- [29] G. B. Cook and M. Zalutskiy, Modes of the Kerr geometry with purely imaginary frequencies, *Phys. Rev. D* **94**, 104074 (2016), [arXiv:1607.07406 \[gr-qc\]](#).
- [30] E. W. Leaver, An Analytic representation for the quasinormal modes of Kerr black holes, *Proc. Roy. Soc. Lond. A* **402**, 285 (1985).
- [31] H. Onozawa, A Detailed study of quasinormal frequencies of the Kerr black hole, *Phys. Rev. D* **55**, 3593 (1997), [arXiv:gr-qc/9610048](#).
- [32] G. B. Cook and M. Zalutskiy, Gravitational perturbations of the Kerr geometry: High-accuracy study, *Phys. Rev. D* **90**, 124021 (2014), [arXiv:1410.7698 \[gr-qc\]](#).
- [33] J. Bezanson, A. Edelman, S. Karpinski, and V. B. Shah, Julia: A fresh approach to numerical computing, *SIAM Review* **59**, 65 (2017).
- [34] J. Verner, Numerically optimal Runge-Kutta pairs with interpolants, *Numerical Algorithms* **53**, 383 (2010).
- [35] C. Rackauckas and Q. Nie, Differentialequations.jl—a performant and feature-rich ecosystem for solving differential equations in julia, *Journal of Open Research Software* **5**, 15 (2017).

- [36] S. A. Hughes, The Evolution of circular, nonequatorial orbits of Kerr black holes due to gravitational wave emission, *Phys. Rev. D* **61**, 084004 (2000), [Erratum: *Phys.Rev.D* 63, 049902 (2001), Erratum: *Phys.Rev.D* 65, 069902 (2002), Erratum: *Phys.Rev.D* 67, 089901 (2003), Erratum: *Phys.Rev.D* 78, 109902 (2008), Erratum: *Phys.Rev.D* 90, 109904 (2014)], [arXiv:gr-qc/9910091](#).
- [37] W. H. Press, S. A. Teukolsky, W. T. Vetterling, and B. P. Flannery, *Numerical Recipes 3rd Edition: The Art of Scientific Computing*, 3rd ed. (Cambridge University Press, USA, 2007).
- [38] A. A. Starobinskii and S. M. Churilov, Amplification of electromagnetic and gravitational waves scattered by a rotating "black hole", *Sov. Phys. JETP* **65**, 1 (1974).
- [39] S. A. Teukolsky and W. H. Press, Perturbations of a rotating black hole. III - Interaction of the hole with gravitational and electromagnetic radiation, *Astrophys. J.* **193**, 443 (1974).
- [40] L. C. Stein, qnm: A Python package for calculating Kerr quasinormal modes, separation constants, and spherical-spheroidal mixing coefficients, *J. Open Source Softw.* **4**, 1683 (2019), [arXiv:1908.10377 \[gr-qc\]](#).
- [41] M. Richartz, Quasinormal modes of extremal black holes, *Phys. Rev. D* **93**, 064062 (2016), [arXiv:1509.04260 \[gr-qc\]](#).
- [42] C. Ridders, Accurate computation of  $F'(x)$  and  $F'(x)F''(x)$ , *Advances in Engineering Software* (1978) **4**, 75 (1982).
- [43] M. Casals and R. T. da Costa, The Teukolsky–Starobinsky constants: facts and fictions, *Class. Quant. Grav.* **38**, 165016 (2020), [arXiv:2102.06734 \[gr-qc\]](#).
- [44] H. Motohashi, Kerr quasinormal mode frequencies and excitation factors, [10.5281/zenodo.14380191](#) (2025).
- [45] N. Oshita and V. Cardoso, Reconstruction of ringdown with excitation factors, (2024), [arXiv:2407.02563 \[gr-qc\]](#).
- [46] H. Yang, F. Zhang, A. Zimmerman, D. A. Nichols, E. Berti, and Y. Chen, Branching of quasinormal modes for nearly extremal Kerr black holes, *Phys. Rev. D* **87**, 041502 (2013), [arXiv:1212.3271 \[gr-qc\]](#).
- [47] B. C. da Cunha and J. a. P. Cavalcante, Teukolsky master equation and Painlevé transcendents: Numerics and extremal limit, *Phys. Rev. D* **104**, 084051 (2021), [arXiv:2105.08790 \[hep-th\]](#).
- [48] O. J. C. Dias, M. Godazgar, J. E. Santos, G. Carullo, W. Del Pozzo, and D. Laghi, Eigenvalue repulsions in the quasinormal spectra of the Kerr–Newman black hole, *Phys. Rev. D* **105**, 084044 (2022), [arXiv:2109.13949 \[gr-qc\]](#).
- [49] L. D. Landau and E. M. Lifshits, *Quantum Mechanics: Non-Relativistic Theory*, Course of Theoretical Physics, Vol. v.3 (Butterworth-Heinemann, Oxford, 1991).
- [50] W. D. Heiss, Repulsion of resonance states and exceptional points, *Phys. Rev. E* **61**, 929 (2000).
- [51] W. D. Heiss, The physics of exceptional points, *J. Phys. A* **45**, 444016 (2012), [arXiv:1210.7536 \[quant-ph\]](#).
- [52] T. Kato, *Perturbation Theory for Linear Operators*, Classics in Mathematics (Springer Berlin Heidelberg, 1995).
- [53] J. a. P. Cavalcante, M. Richartz, and B. C. da Cunha, Exceptional Point and Hysteresis in Perturbations of Kerr Black Holes, *Phys. Rev. Lett.* **133**, 261401 (2024), [arXiv:2407.20850 \[gr-qc\]](#).
- [54] M. Casals and L. F. Longo Micchi, Spectroscopy of extremal and near-extremal Kerr black holes, *Phys. Rev. D* **99**, 084047 (2019), [arXiv:1901.04586 \[gr-qc\]](#).
- [55] G. Aminov, A. Grassi, and Y. Hatsuda, Black Hole Quasinormal Modes and Seiberg–Witten Theory, *Anales Henri Poincaré* **23**, 1951 (2022), [arXiv:2006.06111 \[hep-th\]](#).
- [56] G. Bonelli, C. Iossa, D. P. Lichtig, and A. Tanzini, Exact solution of Kerr black hole perturbations via CFT2 and instanton counting: Greybody factor, quasinormal modes, and Love numbers, *Phys. Rev. D* **105**, 044047 (2022), [arXiv:2105.04483 \[hep-th\]](#).
- [57] R. Panosso Macedo, Hyperboloidal framework for the Kerr spacetime, *Class. Quant. Grav.* **37**, 065019 (2020), [arXiv:1910.13452 \[gr-qc\]](#).
- [58] K. Glampedakis, A. D. Johnson, and D. Kennefick, Darboux transformation in black hole perturbation theory, *Phys. Rev. D* **96**, 024036 (2017), [arXiv:1702.06459 \[gr-qc\]](#).